Chemical Geology 683 (2025) 122759

Contents lists available at ScienceDirect

Chemical Geology

journal homepage: www.elsevier.com/locate/chemgeo

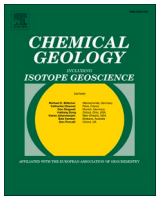

Subduction and melting of biogenic and ferromanganese sediments as evidenced by sub-Moho granitoids

Tiago Valim Angelo [a,*], Christopher J. Spencer [a], Hong-Yan Li [b], Derek Knaack [a], Ziyi Zhu [c], Marina Seraine [a,d], Nick M.W. Roberts [e], Evelyne Leduc [a], Sophie Divilek [a], Anna Ren [a], Brian Joy [a], Gui-Mei Lu [f]

[a] Department of Geological Sciences and Geological Engineering, Queen's University, Kingston, ON K7L 3N6, Canada
[b] State Key Laboratory of Deep Earth Processes and Resources, Guangzhou Institute of Geochemistry, Chinese Academy of Sciences, Guangzhou 510640, China
[c] School of Earth, Atmosphere and Environment, Monash University, Melbourne VIC3168, Australia
[d] Timescales of Mineral Systems Group, Curtin Frontier Institute of Geoscience Solutions, School of Earth and Planetary Sciences, Curtin University, Perth WA 6845, Australia
[e] Geochronology and Tracers Facility, British Geological Survey, Nottingham NG12 5GG, United Kingdom
[f] State Key Laboratory of Isotope Geochemistry, Guangzhou Institute of Geochemistry, Chinese Academy of Sciences, Guangzhou, 510640, China

ARTICLE INFO

Editor: S Aulbach

Keywords:
Samail ophiolite
Granitoids
Isotopes
Petrogenesis
Ferromanganese sediments
S-type granitoids
Supra-subduction

ABSTRACT

Mantle-hosted granitoids (MHG) from the supra-subduction Samail ophiolite in Oman and the United Arab Emirates exhibit diverse compositions, highlighting variations in petrogenesis and source contributions. Previous isotopic data indicate these MHG originated through the interaction of sediment-derived with basaltic melts from an underthrust oceanic plate within the mantle wedge. The sedimentary contribution was attributed to the partial melting of pelitic to siliceous (bio-siliceous) material atop the subducted plate based on elevated zircon $\delta^{18}O$ values (~14–28 ‰). To further evaluate this hypothesis on Samail MHG petrogenesis and source contribution, we present new and compiled radiogenic (Sr-Nd-Hf-Pb) and stable (O-Li-H) isotopes, along with zircon trace element analyses. The variable Sr and Pb isotopic signature support a mixed origin involving altered mafic and sedimentary sources in the formation of the MHG. Negative whole-rock εNd, coupled with elevated $\delta^{7}Li$ in muscovite suggest the involvement of sedimentary sources and particularly those resembling deep-sea ferromanganese-rich sediments. We propose a new model identifying ferromanganese sediments as a potential source given their widespread distribution across the ocean floor, broad range of $\delta^{18}O$ (up to 29.5 ‰), slightly positive Hf values, seawater-like $\delta^{7}Li$ signatures (median of ~27 ‰), and zircon trace element compositions lacking a signature of monazite co-precipitation, which match the signatures required for the genesis of the Samail MHG. Preservation of oceanic lithosphere in the geological record is limited, and MHG in ophiolites are uncommon. Therefore, the Samail MHG are key examples of crustal materials transported to the mantle, with implications for mantle heterogeneity and arc mantle redox budget.

1. Introduction

Investigating granitoids formed in subduction zone environments is vital for unravelling the origins of continental crust and the compositional evolution of the mantle. Emerging subduction systems are often well-preserved within supra-subduction zone (SSZ) ophiolites, where the rapid onset of subduction and extension of the upper plate generate oceanic crustal rocks with distinctive compositional characteristics specific to this setting (Hawkins, 2003; Metcalf and Shervais, 2008). Various types of granitoid intrusions with evolved chemical signatures are common in SSZ ophiolites. For example, diorite to tonalite, trondhjemite and granite intrusions in ophiolite systems are well-known and have been mapped along the length of ophiolite settings in the crustal section (Bailey, 1981; Freund et al., 2014; Haase et al., 2016; Koepke et al., 2007; Lippard et al., 1986), as well as scarce felsic sills, dykes, and plugs mostly in the uppermost mantle section and rare intrusions in the lower crust (Adachi and Miyashita, 2003; Al Humadi et al., 2021; Amri et al., 2007, 1996; Haase et al., 2015; Rioux et al.,

* Corresponding author.
E-mail address: tiago.angelo@queensu.ca (T.V. Angelo).

https://doi.org/10.1016/j.chemgeo.2025.122759
Received 9 February 2025; Received in revised form 25 March 2025; Accepted 26 March 2025
Available online 1 April 2025

2021a; Rollinson, 2014; Rollinson and Adetunji, 2015; Styles et al., 2006; Whitehead et al., 2000).

The Samail ophiolite in Oman and the United Arab Emirates (UAE) is one of the best-exposed and least-deformed subaerial sections of oceanic crust, providing an excellent example to study subduction-related granitoids. It consists of a ~ 5 km crustal section (Nicolas et al., 1996) with pillow basalt, sheeted dikes, and gabbro underlain by a mantle section composed of peridotite (harzburgite). During the Late Cretaceous, this oceanic crust and mantle were obducted onto the Upper Paleozoic-Mesozoic passive margin of the Arabian plate. The Samail ophiolite is interpreted as a classic SSZ system (Dilek and Furnes, 2009; Pearce et al., 1981; Searle and Cox, 1999; Searle and Malpas, 1980; Warren et al., 2005), where granitoids intruding the crustal section formed at the spreading ridge (Amri et al., 1996; France et al., 2009; Koepke et al., 2004; Rollinson, 2009) while granitoids hosted in the uppermost mantle section and rare intrusions in the lower crust formed by hydrous partial melting of the descending slab with its sediment cover (Haase et al., 2015; Rollinson, 2015).

Despite their prevalence, the variable composition of the granitoids hosted in the mantle section of the Samail ophiolite has made their formation and source(s) difficult to be fully understood. These granitoids exhibit characteristics aligning with S-type classification parameters (Chappell and White, 1974). These Samail granitoids are relatively potassic, have peraluminous characteristics [$Al_2O_3/(CaO + Na_2O + K_2O) > 1$] (Angelo et al., 2023) and occasionally contain aluminous phases such as garnet, andalusite, cordierite, and muscovite. They also display high $\delta^{18}O$ values (Kim et al., 2020; Spencer et al., 2017), and crustal Nd and Hf signatures (Haase et al., 2015; Rioux et al., 2021a). Furthermore, comparisons of their elemental geochemistry with S-types from classic localities (e.g., Lachlan Fold Belt, Himalayan orogen, and Variscan orogen) reveal some similarities (Angelo et al., 2023; Bonin et al., 2020). The MHG are thought to be formed by melting of metasediment and amphibolite from an underthrust sheet of oceanic lithosphere (Boudier et al., 1988; Briqueu et al., 1991; Haase et al., 2015; Rioux et al., 2013; Rollinson, 2015, 2014, 2009; Spencer et al., 2017). Three-component model invokes mixing between melts of metasedimentary and metabasaltic rocks generated near the top of a subduction plate, along with a mantle component (Amri et al., 2007; Boudier et al., 1988; Briqueu et al., 1991; Haase et al., 2015; Peters and Kamber, 1994; Rioux et al., 2021a). In this model, the identity of the metasedimentary protolith remains unclear, although previous studies restrict the melt source to high $\delta^{18}O$ pelagic and/or siliceous mud (Spencer et al., 2017). The compositional diversity in terms of elemental geochemistry and stable (oxygen) and radiogenic isotope (Nd and Hf) signatures pointed out by previous authors (Angelo et al., 2023; Rioux et al., 2021a) justify the re-evaluation of the available isotopic and trace element data regarding these mantle-hosted granitoids (MHG; as we refer to them here in this study) from the Samail ophiolite. Recent studies have suggested that stable isotopic compositions may be useful tracers of magma sources (e.g., Tomascak, 2004; Kemp et al., 2007; Spencer et al., 2017) to be complemented by traditional radiogenic isotopic tracers of petrogenesis.

In this paper, we present new and published radiogenic (Sr-Nd-Hf-Pb) and stable (O-H-Li) isotopes coupled with new zircon trace element data for the compositionally diverse MHG suite from the Samail ophiolite. We discuss possible source(s) and petrogenesis of these intrusions in the context of their unique tectonic setting and emplacement. Whereas previous work has postulated the involvement of a sedimentary protolith of a deep-sea pelagic and/or siliceous nature (Haase et al., 2015; Spencer et al., 2017), we argue that our new data suggest ferromanganese (Fe-Mn) crusts and precipitates (Fe-Mn sediments) – chemical precipitates that are widespread in the global ocean – as a potential source. Our integrated data provides new perspectives on the source of the MHG and valuable petrogenetic insights in the realm of S-type granitoids, and our findings show that combining radiogenic and stable isotopes with zircon trace element data offers valuable petrogenetic insights into the formation of sediment-derived granitoids.

2. Geologic setting

2.1. The Samail ophiolite in Oman and the United Arab Emirates

The Samail ophiolite extends for almost 500 km along the Gulf of Oman (Fig. 1) and covers >20,000 km^2 (Lippard et al., 1986). It preserves a complete section of relatively undeformed Cretaceous oceanic lithosphere, from mantle peridotite below the petrologic Moho to crustal layered gabbro, isotropic gabbro, sheeted dykes, and basalt pillow lavas, with intercalated pelagic sediments, all lying on top of a fault-bound metamorphic-sole (Nicolas et al., 2000). The oceanic crust of the Samail ophiolite (Glennie et al., 1973) formed at ca. 96 Ma (Goodenough et al., 2010; Rioux et al., 2021b, 2012) and was later obducted onto a middle Permian to middle Cretaceous shelf carbonate sequence on the Arabian passive continental margin at ca. 84 Ma (Dilek and Furnes, 2009; Glennie et al., 1973; Goodenough et al., 2014; Searle and Cox, 1999, 2002). Goodenough et al. (2010) recognize two distinct phases of magmatism in the UAE part of the ophiolite. Phase 1 consists of the classic ophiolite section as described above. The younger Phase 2 magmatism consists of voluminous isotropic gabbro, wehrlite, and granitoids. Phase 2 crosscut Phase 1 peridotite and crustal ophiolite sequence. The same phases of magmatism have been described in Oman (Adachi and Miyashita, 2003; Tsuchiya et al., 2013).

Two distinct suites of granitoids have been recognized in the Samail ophiolite, based on their composition and occurrence within the mantle and the crustal sequence. Granitoid dykes ranging from 1 to 10 m in width, sheets, and small plutons up to 1 km in size have been mapped in both the basalt-gabbro-dominated ocean crust as well as within peridotite-dominated mantle sections (Amri et al., 1996; Briqueu et al., 1991; Browning and Smewing, 1981; Cox et al., 1999; Haase et al., 2015; Lippard et al., 1986; Rioux et al., 2021a; Rollinson, 2015; Spencer et al., 2017; Stakes and Taylor, 2003; Styles et al., 2006). These intrusions are referred here as the crust-hosted granitoids (CHG) and the mantle-hosted granitoids (MHG), respectively, the latter of which is the focus

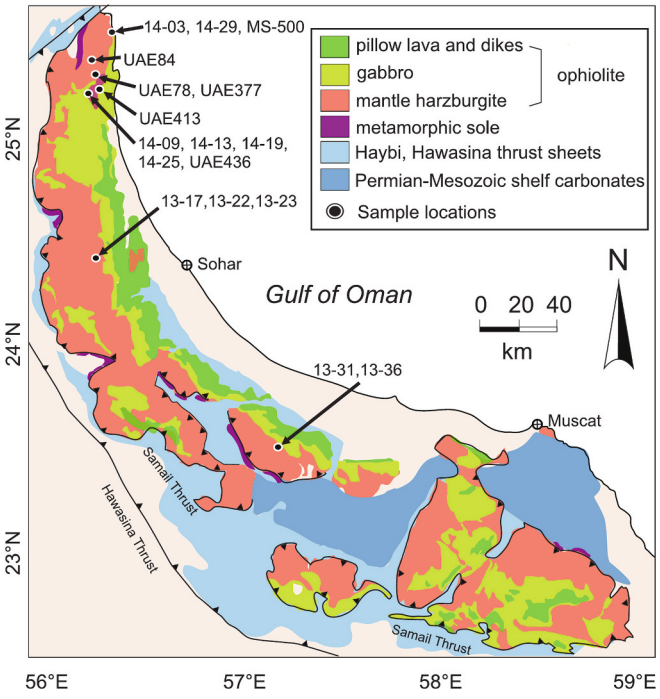

Fig. 1. Simplified geologic map of the Oman-United Arab Emirates (UAE) ophiolite (after Glennie et al., 1974) with sample locations employed in this study.

of this study.

The CHG have been previously referred to as the 'crustal plagiogranite' suite (Rollinson, 2009). The predominant petrographic type consists of medium- to coarse-grained tonalite- trondhjemite-granodiorite. They contain plagioclase and quartz, minor alkali feldspar, interstitial amphibole and clinopyroxene (highly altered to chlorite and/or epidote). Textures are mostly defined by quartz and feldspar and range from subhedral granular to granophyric (de Graaff et al., 2019; Lippard et al., 1986; Rollinson, 2009). The CHG are metaluminous, with SiO_2 ranging from 54 to 72 wt%, and low K_2O (<1 wt%). Trace elements are slightly LREE-depleted compared to mantle-hosted granitoids (Rollinson, 2014, 2009). The CHG with zircon $\delta^{18}O$ of 4–5 ‰, whole rock $\delta^{18}O$ of 5–13 ‰ and positive εNd of around +7 (similar to modern mid-ocean ridges), likely formed by fractionation of basalt/gabbro or anatexis of oceanic crust (Alberts, 2016; Amri et al., 1996; Grimes et al., 2013; Koepke et al., 2004; Rollinson, 2015, 2009; Spencer et al., 2017; Stakes and Taylor, 2003, Stakes and Taylor, 1992). Tonalite and trondhjemite samples of the CHG yield zircon U-Pb ages between 95.4 and 95.7 Ma (Goodenough et al., 2010; Grantham et al., 2003; Rioux et al., 2021b, Rioux et al., 2013; Rioux et al., 2012; Styles et al., 2006; Tilton et al., 1981).

The MHG intrude the uppermost mantle, where they are recognized as sub-Moho granitoids, and rarely extend into the lower crust. These granitoids are highly unexpected due to their isotopic composition and occurrence within the mantle section. While plagiogranites are common in ophiolites and at modern mid-ocean ridges, MHG represent an unusual suite that requires further investigation. While both granitoid suites are significant, the distinction between them is crucial. The following section provides a detailed examination of the characteristics and petrogenesis of the MHG.

2.1.1. Samail ophiolite mantle-hosted granitoids (MHG)

The representative petrologic type of the MHG is medium to coarse-grained, with subhedral to anhedral primary granular textures, and ranges from granite to tonalite in composition. Primary minerals include plagioclase, quartz, alkali feldspar, hornblende, biotite, muscovite, clinopyroxene, and Fe-Ti oxides (Joun et al., 2019; Rollinson, 2015; Rollinson et al., 2014). Certain intrusions in the northern UAE are identified as leucogranites containing garnet, andalusite, cordierite, and tourmaline (Rollinson, 2015). Plagioclase in these rocks often exhibits zoning, with sericitized cores being a common feature (Lippard et al., 1986; Rollinson, 2014; Spencer et al., 2017). The MHG display SiO_2 concentrations between 65 and 78 wt% and range from metaluminous to peraluminous compositions (Briqueu et al., 1991; Cox et al., 1999; Peters and Kamber, 1994; Rioux et al., 2021a; Rollinson, 2015, 2014; Searle et al., 2015). U-Pb zircon dating with high precision indicates that most MHG intrusions occurred between 95.2 and 95.0 Ma during the late stages of crustal growth, with one slightly earlier event at 95.5 Ma (Rioux et al., 2021b). Some intrusions within the UAE are considerably younger, dated between 94.1 and 91.0 Ma (Rioux et al., 2021b; Styles et al., 2006).

The petrogenesis of the MHG from the Samail ophiolite remains controversial, as well as the uncertain nature of the sedimentary protolith that contributed to its formation. Previous studies in the eighties (Browning and Smewing, 1981; Lippard et al., 1986), suggested that biotite granite intrusions in the upper mantle in the UAE reflect melting of continental material during the obduction of the ophiolite over the Arabian passive margin. Later in the nineties (Briqueu et al., 1991; Cox et al., 1999), isotopes and whole-rock data showed that the felsic mantle dykes in the UAE have an intermediate composition between a mantle source and continental values. The formation of these dykes was attributed to melting of amphibolite and metasediments in the metamorphic sole of the ophiolite, during the initial thrusting of the ophiolite over the adjacent continental crust. In the Oman section of the ophiolite, mixing between a depleted mantle source, a hydrothermal component, and potentially a component of terrigenous sediment was suggested based on whole-rock and Nd-Sr isotopic compositions (Amri et al., 2007). A more recent study using Hf isotopes in Oman MHG argues for two-component mixing between sediment melts derived from the top of a subducting slab and basalts formed by partial melting of the overlying mantle wedge (Haase et al., 2015). Three-component mixing between partial melts derived from amphibolite- to granulite-facies meta-basalts in a subducted slab, partial melts of subducted sediment from the top of the slab, and assimilation of orthopyroxene and amphibole from harzburgites during accent of the slab melts through the mantle wedge was suggested in more detailed studies for MHG samples (Rollinson, 2015, 2014). Quantification by geochemical modeling of the protolith using least MHG fractionated samples indicate 10–30 % of mixing of a metasedimentary melt into the melt of a mafic source in the measured granitoid compositions.

Spencer et al. (2017) show that the oxygen isotopic composition of MHG from Oman and the UAE record extremely elevated zircon $\delta^{18}O$ values ranging from ~14–28 ‰, which have been attributed to melting of pelitic or siliceous sediment. The zircon data are further supported by whole-rock and quartz $\delta^{18}O$ values, which are 7–19 ‰ and 7–22 ‰, respectively (Alberts, 2016; Spencer et al., 2017). Terrigenous sediment input is suggested by variable εNd values in the MHG, ranging from −7.8 to 8.3 with a mean of −3.2 (Amri et al., 2007; Cox et al., 1999; Haase et al., 2015; Rioux et al., 2021a). In summary, the MHG were generated from an underthrust sheet of oceanic lithosphere by three distinct mixing and fractionation trends: (i) three-component mixing between sediment melt, amphibolite melt and a mantle component; (ii) two-component mixing between amphibolite and sediment melts, with little mantle contribution; and (iii) fractional crystallization of depleted, mantle-derived magmas (Amri et al., 2007; Boudier et al., 1988; Briqueu et al., 1991; Haase et al., 2015; Peters and Kamber, 1994; Rioux et al., 2021a). Low MgO (<1 wt%) associated with low Ni, high SiO_2, and εNd ranging from −6 to +4; (Rioux et al., 2021a) were suggested to represent two-component mixing between partial melts of amphibolite- to granulite-facies metasedimentary and metabasaltic sources. MHG with higher MgO (>1 wt%) and Ni, together withs lower SiO_2 and εNd ranging from −6 to −4 (Rioux et al., 2021a) reflect mixing between metabasaltic/metasedimentary melts and a mantle component. Combined geochemical and pseudosection modeling (Rioux et al., 2021a) suggests the MHG were generated by partial melting of underthrust material at $P \leq 1.4$ GPa and $T \geq 700$–$750°$. The extremely high $\delta^{18}O$ values, synchronous MHG intrusion with ocean crust formation predating obduction and uncertainty of the magmatic sources, prompted us to reevaluate their protoliths through additional isotopic and compositional (zircon trace elements) data.

3. Sampling and analytical methods

We present new whole-rock Sr-Nd-Pb-Hf isotopes, zircon O, Hf isotopes and trace elements, quartz O isotopes, and muscovite Li and H isotopes data for the Samail MHG. Samples can be classified as tonalite, trondhjemite, granodiorite and granite (sensu *strictu*) based on normative An-Ab-Or (Angelo et al., 2023; Rollinson, 2015). The new MHG data (total of 65 new samples analyses) expand the number of localities analyzed for these isotopes in the ophiolite. Tables and figures referred to in the text with an SM- prefix are available in the Supplementary Material. Supplementary Material A contain supplementary figures cited in the text and complementary analytical methods information. Supplementary Materials B and C are Excel files containing new (Tables SM1) and compiled (Tables SM2) data necessary to this study, respectively. Analyzed petrologic types vary from medium to coarse-grained, with subhedral to anhedral primary granular textures marked by plagioclase, alkali feldspar, quartz, biotite, muscovite, garnet, lepidolite, tourmaline and zircon (Figure SM1 and SM2). Plagioclase in many samples exhibits optically dark and inclusion-rich cores with euhedral rims. For our methods, besides whole-rock fractions, we used quartz, muscovite and zircon. Quartz is most readily distinguished by its lack of

color, cleavage and visible twinning. It is typically fresh and unaltered and presents a vitreous luster. Muscovite is characterized by thin, platy sheets with perfect cleavage. Generally, it has a silvery luster and ranges in color from colorless to pale grey; some varieties show pinkish hues, mostly in the coarse-grained petrologic types (Figure SM1). Zircon crystals exhibit magmatic zoning patterns (Figure SM3).

In addition, we complement our work with zircon trace element analyses from ten Himalayan S-type granitoid samples from Bhutan, collected and described by Hopkinson (2016) and Hopkinson et al. (2017). These samples are described as leucogranites and are interpreted to represent pure sediment-derived melts based on O-Hf isotopic signatures. They do not record any mantle contribution and provide an 'end-member' of S-type granitoid composition.

3.1. Whole-rock Sr-Nd-Pb-Hf isotopes using MC-ICP-MS

A total of 17 samples of the Samail MHG were analyzed for whole-rock Sr-Nd-Pb-Hf isotopes (Table SM1a). All samples went through sample digestion (except for Nd isotopes) and column chemistry procedures before analyses performed on a Neptune Plus Multi Collector Inductively Coupled Plasma Mass Spectrometry (MC-ICPMS; Thermo Fisher Scientific, Dreieich, Germany) at the Wuhan Sample Solution Analytical Technology Co., Ltd., Hubei, China.

Analyses of the NIST 987 standard solution yield $^{87}Sr/^{86}Sr$ ratio of 0.710242 ± 14 (2SD, $n = 345$), which is identical within error to their published values 0.710248 ± 12 (Zhang and Hu, 2020). In addition, the USGS reference materials BCR-2 (basalt) and RGM-2 (rhyolite) yielded results of 0.705012 ± 22 (2SD, $n = 63$) and 0.704173 ± 20 (2SD, $n = 20$) for $^{87}Sr/^{86}Sr$, respectively, which is identical within error to their published values (Li et al., 2012; Zhang and Hu, 2020).

Analyses of the GSB 04–3258-2015 standard yield $^{143}Nd/^{144}Nd$ ratio of 0.512440 ± 6 (2SD, $n = 31$), which is identical within error to their published values (0.512438 ± 6 (2SD) (Li et al., 2017)). In addition, the USGS reference materials BCR-2 (basalt) and RGM-2 (rhyolite) yielded results of 0.512641 ± 11 (2SD, $n = 82$) and 0.512804 ± 12 (2SD, $n = 80$) for $^{143}Nd/^{144}Nd$, respectively, which is identical within error to published values (Li et al., 2012).

Because of the difference in the mass bias behaviors between Pb and Tl, all measured $^{20x}Pb/^{204}Pb$ ratios of unknown samples were normalized to the well-accepted NIST 981 values of $^{208}Pb/^{204}Pb = 36.7262 \pm 31$, $^{207}Pb/^{204}Pb = 15.5000 \pm 13$, $^{206}Pb/^{204}Pb = 16.9416 \pm 13$ ($n = 119$ (Baker et al., 2004)). One NIST 981 standard was measured every ten samples analyzed. Analyses of NIST 981 standard yielded external precisions of 0.03 % (2RSD) for $^{20x}Pb/^{204}Pb$ ratios. In addition, the USGS reference materials BCR-2 (basalt) yielded results of $^{208}Pb/^{204}Pb = 38.736 \pm 17$, $^{207}Pb/^{204}Pb = 15.628 \pm 3$, $^{206}Pb/^{204}Pb = 18.756 \pm 10$ (2SD, $n = 22$), respectively, which match their published values within error of 0.03 % (Zhang and Hu, 2020).

Analyses of the JMC 475 standard yielded $^{176}Hf/^{177}Hf$ ratio of 0.282154 ± 5 (2SD, $n = 67$), which is identical within error to their published values (0.282157 ± 16 (Zhang and Hu, 2020)). In addition, the USGS reference materials BCR-2 (basalt) yield results of 0.282864 ± 14 (2SD, $n = 19$) for $^{176}Hf/^{177}Hf$, respectively, which is identical within error to their published values (Zhang and Hu, 2020).

Lu-Hf and Sm-Nd T_{DM} ages for whole-rock samples were calculated based on two-stage model using a $^{176}Lu/^{177}Hf$ value of 0.012 (Rudnick and Gao, 2003) and $^{147}Sm/^{144}Nd$ of 0.12 (Liew and Hofmann, 1988) for the average continental crust, respectively.

3.2. Hafnium isotopes in zircon using LA-ICPMS

A total of 12 samples of the Samail MHG were analyzed for zircon Hf isotopes (Table SM1b) at the John de Laeter Research Centre, Curtin University. Individual zircon grains (mounted and polished in 1-in. epoxy rounds) were ablated using a Resonetics RESOlution M-50 A-LR, incorporating a Compex 102 excimer laser. Isotopic intensities were measured using an Agilent 7700 s quadrupole ICP-MS and a Nu Instruments Plasma II MC-ICP-MS. Reference zircon Mudtank was used to monitor the accuracy and precision of internally corrected (using $^{179}Hf/^{177}Hf = 0.7325$) Hf isotope ratios. 91500 and Plešovice were used as secondary standards. The weighted average ratios of $^{176}Hf/^{177}Hf$ are 0.282299 ± 0.000021 (MSWD = 1.1, n = 8; self-normalized) for 91500, 0.282507 ± 0.000028 (MSWD = 0.22, n = 8) for Mudtank, and 0.282474 ± 0.000011 (MSWD = 1.3, $n = 12$) for Plešovice. These results agree with accepted values (Fisher et al., 2014). The stable $^{178}Hf/^{177}Hf$ and $^{180}Hf/^{177}Hf$ ratios for the reference materials yielded values of 1.46709 ± 0.00006 and 1.88682 ± 0.00010, respectively. Lu-Hf T_{DM} zircon ages were calculated based on two-stage model using a $^{176}Lu/^{177}Hf$ value of 0.012 (Rudnick and Gao, 2003).

3.3. Oxygen isotopes in zircon using SIMS

The oxygen isotope analyses of zircon concentrate from seven Samail MHG (55 individual spot analyses) are reported in Table SM1c. Zircon was separated using standard techniques (i.e., disaggregating, heavy liquids (NaPT and MI), Franz magnetic separation), mounted in epoxy resin and polished to expose a cross section through the center of the grains. Zircons were imaged using cathodoluminescence (CL) and secondary electron (SE) imaging at Curtin University (Fig. SM3) using a MIRA3 field emission scanning electron microscope. Zircon oxygen isotopes were measured via secondary ion mass spectrometry (SIMS). We used a CAMECA 1270 ion microprobe at the Edinburgh Ion Microprobe Facility (EIMF), University of Edinburgh and a CAMECA 1280 microprobe at the Centre for Microscopy, Characterization and Analysis at the University of Western Australia (CMCA).

For zircon SIMS analysis, $\delta^{18}O$ was measured using a 15 μm spot (EIMF and CMCA) and reference materials were analyzed repetitively to bracket sample analyses. At EIMF, zircon references used were Laura, an in-house material with $\delta^{18}O$ by laser fluorination = 5.3 ‰ and 91500 with $\delta^{18}O$ = 9.9 ‰ (Wiedenbeck et al., 2004). At CMCA, zircon references used were Laura ($\delta^{18}O = 5.3 \pm 0.1$ ‰, in-house at EIMF), Temora 2 [$\delta^{18}O = 8.2 \pm 0.3$ ‰ (2 s)], Penglai [$\delta^{18}O = 5.2 \pm 0.3$ ‰ (2 s)], BR266 [$\delta^{18}O = 13.1 \pm 0.5$ (2 s) ‰] and GJ1 [$\delta^{18}O = 6.2 \pm 0.5$ ‰ (2 s)]. Our results agree with accepted values (Li et al., 2010; Liebmann et al., 2023; Stern, 2001; Valley, 2003; Wiedenbeck et al., 2004; Xia et al., 2019).

3.4. Oxygen isotopes in quartz using IRMS

The oxygen isotope analyses of quartz concentrate from five Samail MHG (Table SM1d) were conducted in the Queen's Facility for Isotope Research (QFIR) at Queen's University, Kingston, Ontario, Canada. Measurements were done using a Thermo-Finnigan Delta^{Plus}XP isotope ratio mass spectrometer (IRMS) after oxygen extraction using BrF_5. Quality assurance and control were maintained by ensuring at least 20 % of analyses were of reference material NBS-28, and by generating duplicate measurements of unknown samples. Reference materials and duplicates were arbitrarily loaded among the reaction vessels of the extraction line to avoid bias in our precision. We report an accuracy (one standard deviation) of 0.1 ‰ based on measurements of NBS-28.

3.5. Zircon trace element measurements and U-Pb dating by LAICPMS

The U-Pb age and trace element data for zircon reference materials and zircons from the Himalayan and Samail samples are provided in Table SM1e. The table comprises zircon from three harzburgite-hosted biotite granite from the Samail ophiolite and ten Himalaya S-type leucogranite and pegmatite. Samples from the Himalayan granitoids complementing this study were collected and described in Hopkinson (2016) and Hopkinson et al. (2017). New zircon trace element measurements from Himalaya granitoids in Bhutan and Samail MHG were mounted in epoxy and imaged by cathodoluminescence (CL) to investigate their internal structure. Representative zircon CL and backscattered electron

(BSE) images from the Samail MHG are shown in figure SM3. Representative CL images of the Himalayan granitoids were published by Hopkinson (2016). The zircon U-Pb and trace element compositions were measured by an Agilent 7500a quadrupole ICPMS (inductively coupled plasma mass spectrometry) coupled to a HelEx ArF excimer laser ablation system, at the Research School of Earth Sciences, the Australian National University.

The primary reference materials for U-Pb isotopic dating and trace element measurements were zircon R33, which has a published age of 419.26 ± 0.39 Ma according to Black et al. (2004), and NIST610 glass (Jochum et al., 2011), respectively (Table SM1e). Temora2, with a published age of 416.78 ± 0.33 Ma (Black et al., 2004), and 91500, with a published age of 1065 ± 0.6 Ma (Wiedenbeck et al., 1995), were analyzed as secondary standards. The 91500 reference material was used as the calibration standard to obtain $^{207}Pb/^{206}Pb$ ratios. $^{207}Pb/^{206}Pb$ ages were generated using the IsoplotR software online (Vermeesch, 2018). For all the reference data collected in this study, R33 yielded an average $^{206}Pb/^{238}U$ age of 418.01 ± 12.34 Ma (2SD, $n = 55$), Temora2 yielded an average $^{206}Pb/^{238}U$ age of 416.17 ± 17.33 Ma (2SD, $n = 30$), and 91500 yielded an average $^{207}Pb/^{206}Pb$ age of 1066 ± 165 Ma (2SD, $n = 59$). The results agree with published results (Black et al., 2004; Wiedenbeck et al., 1995).

3.6. Lithium isotopes in muscovite using MC-ICPMS

The lithium isotope analyses of muscovite concentrate from five Samail MHG (Table SM1f) were conducted at QFIR values using a Thermo Finnigan Neptune MC-ICPMS. Li-bearing mica (lepidolite) is known to be present in the samples based on previous characterization and petrographic analysis (Figure SM2 and SM3). Two reference materials were also analyzed to evaluate the precision and accuracy of measurements. An in-house Li standard (SPEC Certiprep Lot #19 11-120LI) yielded δ^7Li of 81.6 ± 0.3 ‰ (SD, n = 5) and the NASS7 yielded a value of δ^7Li of 30.9 ± 0.7 ‰ (SD, n = 3). Both are consistent with previously published values (Li et al., 2019; Nadeau et al., 2021).

3.7. Elemental composition in muscovite using EPMA

Muscovite major and minor elements of two MHG samples (HD and 19UAE08C) were determined using electron-probe micro analyzer (EPMA) housed at QFIR. First, muscovite crystals were identified and imaged (Figure SM5) using the backscattered electron (BSE) detector of a JEOL (Japan Electron Optics Laboratory) JXA-8230 electron microprobe. A total of 44 EPMA spots (Table SM1g) were analyzed by means of wavelength dispersive spectroscopy (WDS) for elemental compositions. Accelerating potential of 15 kV, beam current of 15 nA, and beam diameter of 7 μm were used for quantitative analyses. Standards used in the analysis were: muscovite (Si), anorthite (Al), rutile (Ti), synthetic Cr_2O_3 (Cr), synthetic V_2O_3 (V), synthetic fayalite (Fe), rhodonite (Mn), forsterite (Mg), sanbornite (Ba), albite (Na), adularia (K), synthetic $RbTiOPO_4$ (Rb), synthetic fluorophlogopite (F), and tugtupite (Cl). The dead-time corrected X-ray data were processed using the PAP atomic number and absorption corrections (Pouchou and Pichoir, 1991), characteristic (Reed, 1990) and continuum (Springer, 1971; Springer, 1967) fluorescence corrections, and mass absorption coefficients (Heinrich, 1987) were performed prior to analysis. Additionally, counting statistics and detection limits were determined in accordance with Williams (1987), but with matrix corrections applied.

3.8. Hydrogen isotopes in muscovite using IRMS

Selected muscovite crystals from seven samples were weighed into silver capsules, degassed for 1 h at 100°C, then crushed and loaded into a zero-blank autosampler. The hydrogen isotopic composition (Table SM1h) was measured using a MAT 253 Stable Isotope Ratio Mass Spectrometer (IRMS) coupled to a Thermo Scientific TC/EA High Temperature Conversion Elemental Analyzer, housed at QFIR. δ^2H values are reported using delta (δ) notation in permille (‰), relative to Vienna Standard Mean Ocean Water (VSMOW). Standard reference materials USGS57 biotite (−91.5 ‰) and USGS58 muscovite (−28.4 ‰) were used to calibrate and normalize the observed data (Qi et al., 2017). Replicate analyses of USGS57 and USGS58 yielded a mean value of −91 ‰ ± 0.9 (SD, $n = 6$) and −27.8 ‰ ± 0.9 (SD, n = 6), respectively.

4. Results

4.1. Whole-rock Sr-Nd-Pb-Hf isotopes and zircon Hf isotopes

The Samail MHG have variable whole-rock $\varepsilon Nd_{(96Ma)}$ ranging from −7.77 to +7.35 with a median of −4.21 (Fig. 2A and 3B), in contrast with the positive median values calculated for whole-rock and zircon $\varepsilon Hf_{(96Ma)}$ (Fig. 2B and 3A), which have medians of +5.13 (ranging from 10.27 to 2.64) and + 2.3 (ranging from −1.78 to +8.43), respectively. Whole-rock $\varepsilon Sr_{(96Ma)}$ have a median of 38.3 (Fig. 2C), with highly variable ratios of $^{87}Sr/^{86}Sr$ from 0.7056 to 0.7169 (Fig. 4B). $^{206}Pb/^{204}Pb$ versus $^{208}Pb/^{204}Pb$ reveals a cluster showing average ratios of ~18.79 and ~ 39, respectively (Fig. 4A). Most of the Samail MHG have whole-rock Sm-Nd T_{DM} ages between 220 Ma and 1376 Ma, with a median of 1040 Ma, and whole-rock Lu-Hf T_{DM} ages from 457 to 890 Ma with a median of 734 Ma. Zircon Lu-Hf T_{DM} ages range from 561 to 1140 Ma with a median of 906 Ma (Fig. 2D).

4.2. Zircon, quartz and whole-rock oxygen isotopes

New oxygen isotope analyses conducted in zircon and quartz are presented in Fig. 2E together with other compiled zircon, quartz and whole-rock $\delta^{18}O$ values from previous studies of the Samail MHG. Frequency diagrams in Fig. 2E show a bimodal distribution with overall lower $\delta^{18}O$ values ranging from 3 to 11 ‰ contrasted by higher values between 12 and 28 ‰, highlighting the diverse oxygen compositions within the Samail MHG suite (also Fig. 5). $\delta^{18}O_{qtz}$ range from 7.03 ‰ to 21.9 ‰, with a median of 17.6 ‰ ($n = 15$). $\delta^{18}O_{whole\text{-}rock}$ values range from 6.6 ‰ to 19.3 ‰, with median of 17.1 ‰. Compiled new and published individual spot analyses of $\delta^{18}O_{zrn}$ range from 2.48 ‰ to 27.1 ‰, with a median of 15.44 ‰ ($n = 266$ individual grains).

4.3. Zircon trace elements

Analyzed zircon trace element geochemistry in grains from the Samail MHG (3 samples; 60 individual analyses) and Himalayan S-type granitoids (10 samples, 43 individual analyses) show enrichment in HREE and depletion of LREE, and prominent Ce anomalies. Ce anomalies in the Himalayan samples are less prominent when compared to the MHG. The Eu anomalies for the Himalayan samples are notably more negative than the MHG. Spider plots normalized to the chondrite are provided in the Supplementary material (Figure SM4).

Following discrimination plots for S-type granitoids using zircon trace element compositions by Roberts et al. (2024), we present plots of log(Th/U) versus log(Ce/U) and U/Ce ratio versus Th concentration (ppm) to distinguish between zircon from the Himalayan S-types and Samail MHG (Fig. 6A). The MHG zircon data forms a distinct cluster around −1.5 in log(Ce/U) and − 0.5 in log(Th/U), exhibiting no overlap with data from Himalayan S-type granitoids, which generally exhibit lower values for both log ratios (Fig. 6A). This differentiation is particularly evident in Fig. 6B, where zircon from the Samail MHG consistently display lower U/Ce ratios of two orders of magnitude than zircon from Himalayan S-types.

4.4. Muscovite elemental composition and Li and H isotopes

Muscovite crystals from the five MHG samples have δ^7Li ranging from 13.9 ‰ to 34.1 ‰ with a mean of 25 ‰. Muscovite geochemical

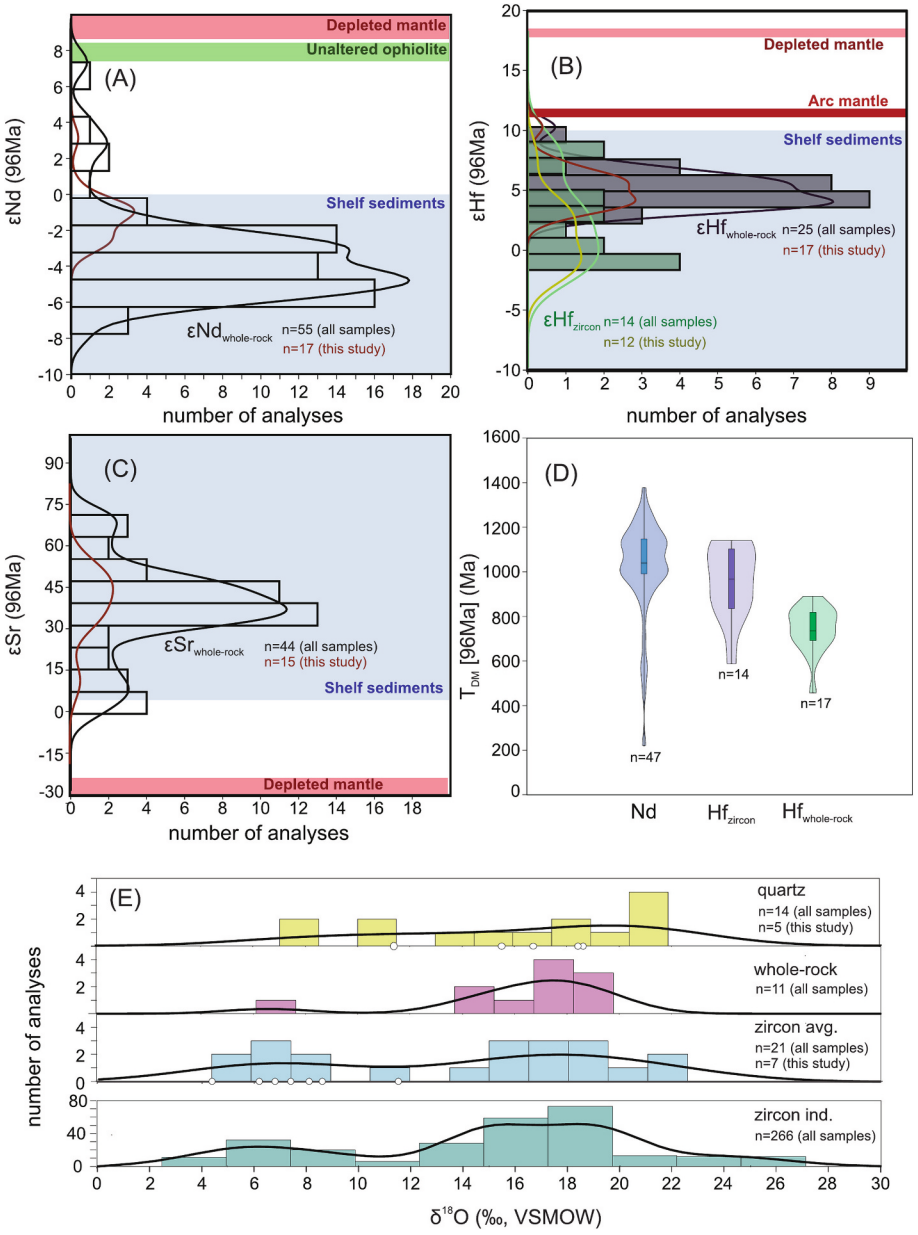

Fig. 2. Histogram plots of initial εNd (A), εHf (B) and εSr (C) for samples from the Samail mantle-hosted granitoids (MHG). They are based on new data from this study and published data from (Alberts, 2016; Kim et al., 2020; Rioux et al., 2021a, 2013). Depleted mantle and unaltered ophiolite fields shown in (A) are from (Kimura et al., 2017) and (McCulloch et al., 1980), respectively. Depleted mantle, arc mantle (Dhuime et al., 2011) plotted for comparison in (B). Depleted mantle field in (C) is from (Kimura et al., 2017; Wilson, 1989). Shelf sediment fields are from (White, 2015). Depleted mantle model ages [$T_{DM(96Ma)}$] ages are shown in panel D. From A to C, kernel density estimation curves are shown for both new and all (compiled) data. Oxygen isotope signatures of quartz, whole-rock and zircon of the Samail MHG are shown in panel E highlighting the variability of oxygen values between samples. Samples obtained from this study are shown as white circles in E. See Table SM1 for data. ind = individual measurements; avg. = average.

data measured in two samples have SiO_2 ranging from 44.6 wt% to 46.3 wt% and Al_2O_3 from 35.9 wt% to 38.8 wt%. These two samples have variable TiO_2 contents, ranging from <0.001 wt% to 0.53 wt%. MgO contents also vary between the two samples significantly, with weight percent mean from 0.08 wt% to 0.22 wt%. δ^2H values of muscovite from six MHG samples range from −47 ‰ to −14 ‰ with a median of −37 ‰.

5. Discussion

5.1. Source diversity within the Samail mantle-hosted granitoids

To better constrain the Samail MHG sources, we combined and compared radiogenic and stable isotopes of the Samail MHG with a range of potential downgoing plate constituents, including fresh and altered ocean crust basalts, marine and hydrothermal sediments, and ocean crust nodules (Table SM2).

Whole-rock, trace elements and isotopic data of the mantle-hosted granitoids indicate a mixed origin between mafic and sedimentary protoliths in a supra-subduction zone setting as proposed previously (e.g., Briqueu et al., 1991; Rollinson, 2014, 2015; Rioux et al., 2021a; Angelo et al., 2023). Evidence of such mixing can be identified by predominantly negative whole-rock $\varepsilon Nd_{(96Ma)}$ (Fig. 2A) and positive $\varepsilon Hf_{(96Ma)}$ (Fig. 2B), which show affinity to sources related to shelf sediments, while the remaining samples with positive $\varepsilon Nd_{(96Ma)}$ values might represent an increasing affinity with an amphibolite component from underthrust sheet of oceanic lithosphere (e.g., Rioux et al., 2021a;

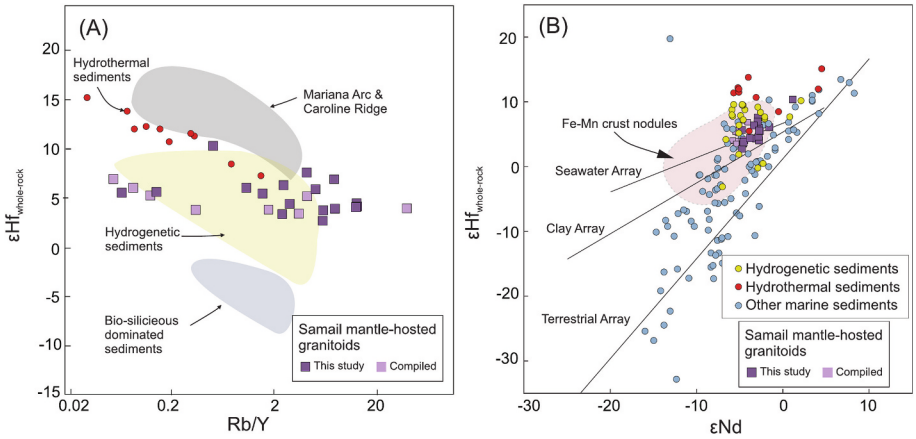

Fig. 3. A) Plot of εHf vs. Rb/Y showing that the Samail MHG fall in the field of the hydrogenetic sediments (Fe-Mn oxyhydroxides bearing source), potentially related to Nd and Hf decoupling of the Samail MHG isotopic signatures. Fields are from Pang et al. (2021) who used data from hydrogenetic sediments (Vervoort et al., 2011) and Mariana Arc and Caroline Ridge volcanic rocks (Pearce et al., 2005; Straub et al., 2015; Woodhead et al., 2001; Zhang et al., 2020). Hydrothermal sediments plotted as red circles are from Pang et al. (2021). B) Whole-rock εHf versus εNd values for the Samail MHG. The Seawater Array (Albarède et al., 1998), the Clay Array (Bayon et al., 2016), and the present-day Terrestrial Array (Vervoort et al., 2011) are shown for comparison. The data from the MHG is from this study and Haase et al. (2015). See table SM2e for compiled Nd-Hf data. (For interpretation of the references to color in this figure legend, the reader is referred to the web version of this article.)

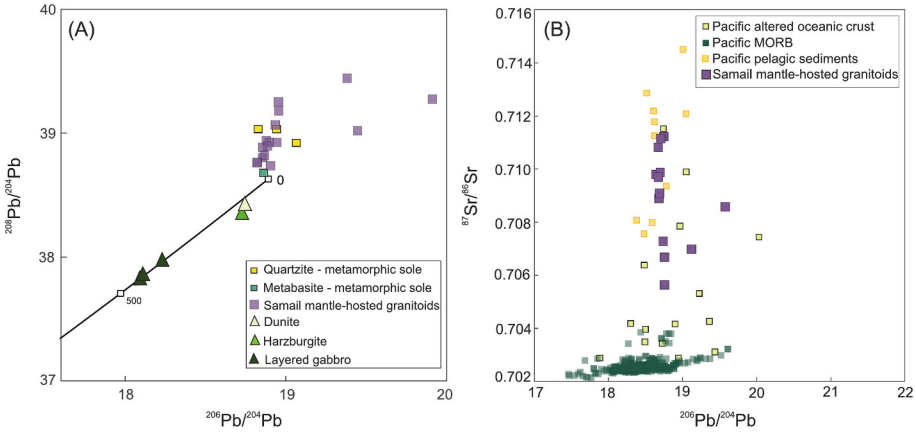

Fig. 4. A) Uranogenic versus thorogenic lead isotope signature of samples from the mantle section of the ophiolite [harzburgite and dunite (Chen and Pallister, 1981)], metamorphic sole [quartzite and metabasite (Briqueu et al., 1991)], and Samail MHG (this study). Stacey and Kramers (1975) model curve was plotted for comparison. The MHG data are consistent with a derivation from older, crustal lead (higher Th/U), similar to the metamorphic sole samples. B) $^{206}Pb/^{204}Pb$ versus $^{87}Sr/^{86}Sr$ for the MHG samples. Pacific altered oceanic crust (Hauff et al., 2003), Pacific MORB (Class and Lehnert, 2012), and Pacific pelagic sediments (Hauff et al., 2003; Plank, 2014) are included for comparisons. See Table SM2f for compiled Sr-Pb data. All data points shown for the MHG are new data generated for this study.

Angelo et al., 2023). The MHG show predominantly elevated whole-rock $\varepsilon Sr_{(96Ma)}$ values (ranging from 0 and + 74; Fig. 2C), $^{208}Pb/^{204}Pb$ (~39) and $^{206}Pb/^{204}Pb$ (~18.5) when compared to negative depleted mantle values and mafic-ultramafic lithologies (Fig. 2C, 4A and B). The MHG Pb isotopic data (Fig. 4A) overlaps with quartzite samples from the metamorphic sole, indicating a significant component of older, crustal lead. A wide range of values of $^{87}Sr/^{86}Sr$ in the MHG samples between 0.705 and 0.711 together with narrow range of $^{206}Pb/^{204}Pb$ averaging around ~18.8 (Fig. 4B) overlaps with the compositions of the Pacific pelagic sediments and altered oceanic crust rocks, further indicating mixing between mafic and sedimentary protoliths.

The derivation from mafic protoliths and mantle components for the MHG is observed in whole-rock, trace elements and isotopic signatures (Angelo et al., 2023; Rioux et al., 2021a; Rollinson, 2015). Here, the lower $\delta^{18}O$ population (<13 ‰) in the MHG (Fig. 5B) overlaps with fields defined by mafic protoliths, including gabbro, sheeted dykes, pillow basalts and mantle-like zircon (Fig. 5A). It also overlaps with zircon composition from the Samail crust-hosted granitoids, which have been interpreted as a result of fractionation of basalt/gabbro or anatexis of oceanic crust (Alberts, 2016; Amri et al., 1996; Grimes et al., 2013; Koepke et al., 2004; Rollinson, 2015, 2009; Spencer et al., 2017; Stakes and Taylor, 2003, 1992).

The contribution of sedimentary protoliths in the Samail MHG sources is supported by the overlapping feature between the MHG and sediments in almost all isotopic systems examined in this study (Sr-Nd-Hf-Pb-O). Predominantly higher εSr, $^{87}Sr/^{86}Sr$, $^{208}Pb/^{204}Pb$, (Figs. 2, 3 and 4) and $\delta^{18}O$ (Fig. 5) and lower εNd and εHf values (Fig. 2) are observed in the MHG when compared to corresponding isotopic signatures from mafic-ultramafic protoliths and lithologies, including the mantle. Oxygen data from the MHG overlap with global shale sediments (Fig. 5), with MHG samples recording the highest $\delta^{18}O$ in zircon values in the igneous record (Spencer et al., 2017). Elevated $\delta^{18}O$ for zircon, quartz and whole-rock ranging from ~12 to ~28 ‰ indicate marine sediments composed of pelite and/or siliceous mud were incorporated during partial melting of metasedimentary rocks on top of the subducted ocean crust during supra-subduction.

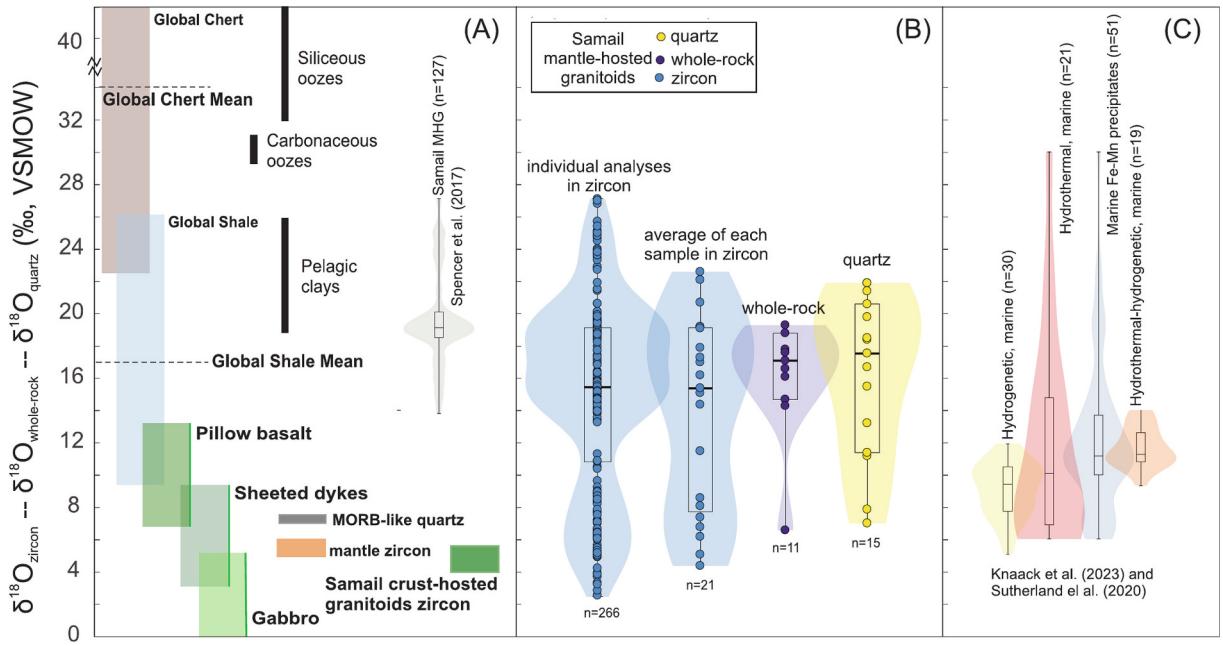

Fig. 5. A) Published ranges of $\delta^{18}O$ values from various sources: zircon from the Samail crust-hosted granitoids (Grimes et al., 2013); whole-rock $\delta^{18}O$ for Phanerozoic global shale (Payne et al., 2015); mantle-like zircon (Valley, 2003); Mid-ocean ridge basalt (MORB)-like quartz (Gregory et al., 1981); pillow basalts, sheeted dykes and gabbro (Gregory et al., 1981; Grimes et al., 2013; Stakes and Taylor, 2003, 1992), and siliceous oozes, carbonaceous oozes and pelagic clays (Valley et al., 2005). Range published by Spencer et al. (2017) for Samail mantle-hosted granitoids is also shown for comparison. B) Combined new and previously published $\delta^{18}O$ for zircon, whole-rock, and quartz from Samail MHG. Two sample populations emerge, one with relatively higher $\delta^{18}O$ ranging from 14 to 23 ‰ and another with lower $\delta^{18}O$ values from 4 to 12 ‰, suggesting a bimodal feature across both mineral phases (zircon and quartz) and whole-rock samples. C) Published $\delta^{18}O$ values for ferromanganese sediments, categorized into hydrogenetic, hydrothermal, and hydrothermal-hydrogenetic showing values up to 30 ‰ (see Table SM2b).

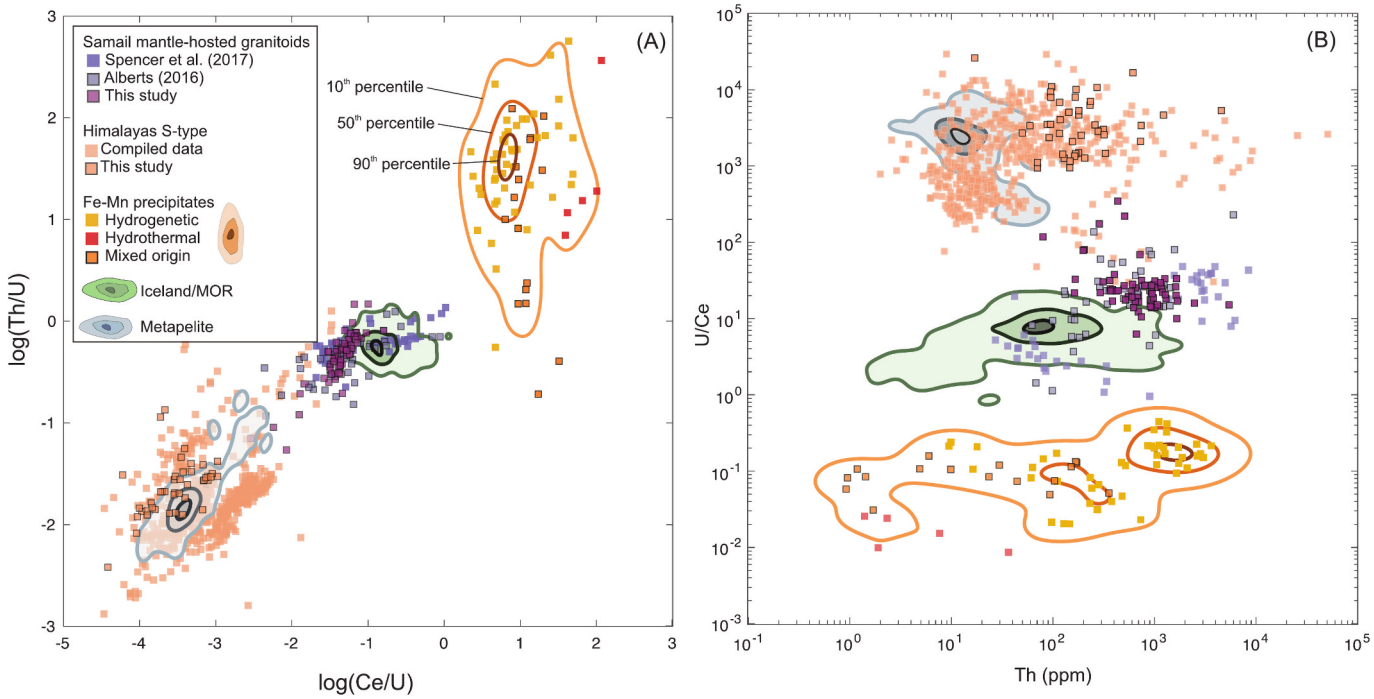

Fig. 6. Scatter plots of A) log(Ce/U) versus log(Th/U) and B) Th (ppm) versus U/Ce for zircon from the Samail mantle-hosted granitoids and Himalayan S-type granitoids compared with contour plots of mantle-derived zircon suites from Iceland/Mid-Ocean Ridges (MOR) and metapelite-derived zircon. Whole-rock trace elements determined in Fe-Mn precipitates of hydrogenetic, hydrothermal and mixed origins are plotted for comparison. See Table SM2c for compiled ferromanganese whole-rock trace element data and Table SM2d for compiled zircon trace element data.

5.2. Deep sea biogenic and Fe-Mn sediments within the Samail ophiolite

Here, we alternatively propose that in addition to biogenic sediments represented by pelagic mud (siliceous and/or pelitic) (Spencer et al., 2017), the melting of marine Fe-Mn precipitates could also explain the isotopic signatures in the MHG.

Zircon grown from or recrystallized via metamorphic reactions exhibit depleted LREE and lower Th/U contents when compared to magmatic/igneous zircon (Martin et al., 2008; Rubatto, 2017; Yakymchuk et al., 2018). The log(Th/U) versus log(Ce/U) discrimination tool (Roberts et al., 2024) makes use of the Th and Ce (LREE) depletion common to anatectic melt and associated zircon in compositions where monazite is stable. As such, these ratios distinguish pure metapelite-derived melts (where monazite is typically stable), which can be considered an end-member of S-type 'sediment-derived' granites (e.g., Himalayan leucogranites), from I-type 'mantle-derived' melts (e.g., MOR and Iceland) with greater log(Th/U) and log(Ce/U) values. Zircon trace element data from the Himalayan samples (Fig. 6A and B) are S-types that completely overlap the metapelite field, indicating they can be considered as pure S-type melts, as previously discussed in Roberts et al. (2024) and Hopkinson et al. (2017). S-types granitoids from other localities have greater overlap with I-type fields ('Hybrid S-types' of Roberts et al., 2024), but the Samail MHG data fall within the fields defined by I-type and other mantle-derived granitoids. As pointed out by Roberts et al. (2024), the Samail MHG do not have zircon compositions equivalent to 'typical' Himalayan-type S-type granitoids. Although a pelitic source has been proposed (Rollinson, 2015; Spencer et al., 2017), no record of monazite as an accessory phase has been identified. In pelitic (metasedimentary) sources, monazite often forms as an accessory mineral because it is a common carrier of REE, especially in aluminum-rich, silica-saturated environments like during partial melting of pelites.

To further understand the MHG compositions, and in turn, the magmatic sources, we compare the zircon compositions with whole-rock compositions of potential sources (see Fig. 6). We note that the Samail MHG zircons have log(Th/U) and log(Ce/U) falling between the Himalayan pure metapelite-derived zircon and the whole-rock composition of the Fe-Mn sediments. We argue that Fe-Mn sediments could have contributed to the formation of the MHG, together with metapelite and metamafic components (Fig. 6A and B). The Samail MHG data in the discrimination plots based in Ce, U and Th support the hybrid nature of the Samail MHG suite, which may have formed through the interaction between metasediment-derived melts with or on top of the mantle-derived ocean crust as previously discussed.

Based on the compilation of zircon trace elements and the given array presented by metapelite and Fe-Mn sediment (Fig. 6A), we hypothesize the presence of a Fe-Mn sediment with a maximum $\delta^{18}O$ of ~28 ‰ that is consistent with the upper endmember of extant Fe-Mn sediment (Fig. 7). The zircon, whole rock and quartz from the MHG generally plot as two different arrays of data, both controlled by $\delta^{18}O$ values paired with mostly positive εHf values. One array demonstrates a less negative correlation with relatively higher $\delta^{18}O$ and greater variability (Fig. 7), with values from ~11 ‰ to 26 ‰. On the other hand, a strongly negative correlation defines the other array, characterized by lower $\delta^{18}O$ values from ~5 ‰ to 10 ‰ (Fig. 7).

Samples of the MHG with lower $\delta^{18}O$ values range from ~4 to 10 ‰ and fall within the fields defined by the 10th percentile of the S-type granitoids from classic localities including the Himalayas, Tasmanides and the Andes (Fig. 7). More than 1400 zircon analyses of coupled $\delta^{18}O$ and εHf from samples of S-types granitoids from these classic localities plot in between and along mixing trends of old lower crust towards, depleted mantle and metasediments. This array suggests some MHG formed through complex processes involving partial melting of subducted MOR-type composition oceanic slab with significant contamination with oceanic sediments that subsequently interacted with hydrothermally altered sub-arc mantle. This is well demonstrated using whole-rock and trace elements (Angelo et al., 2023; Rollinson, 2015), Hf isotopes (Haase et al., 2015) and Nd isotopes (Rioux et al., 2021a). In contrast, the MHG samples with higher $\delta^{18}O$ values do not align with fields defined by zircon from sedimentary-derived granitoids from classic localities. The plot of O and Hf isotopes in fig. 7 clearly shows that most of the MHG was derived from a metasediment protolith that differs compositionally from the sources of classic S-type granitoids.

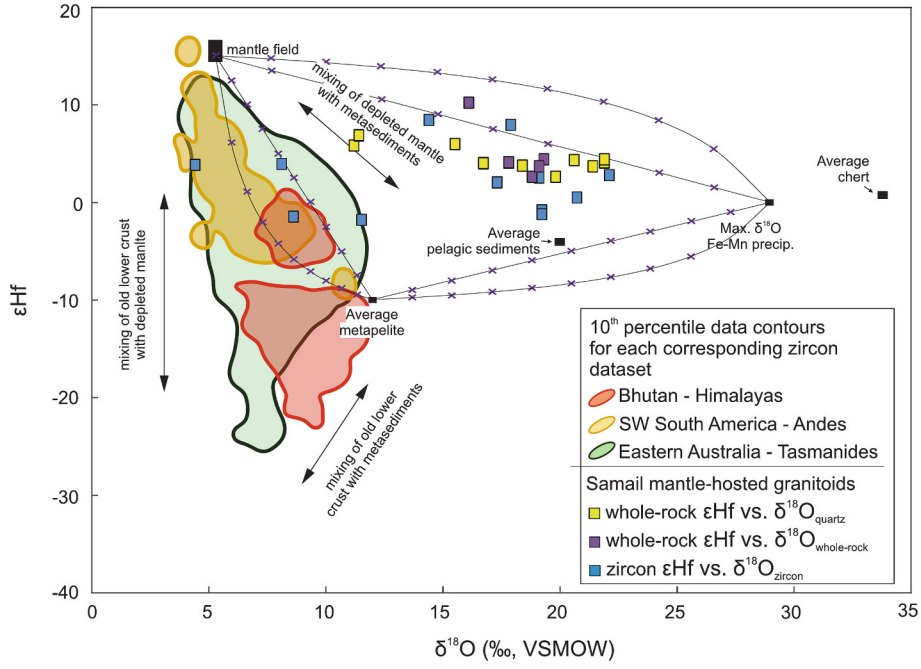

Fig. 7. εHf versus $\delta^{18}O$ for detrital and igneous zircon from classic localities of S-type granitoid formation, including the Himalayas ($n = 259$) (Hopkinson et al., 2017), Tasmanides ($n = 589$) (Dhuime et al., 2012; Jeon and Williams, 2018; Jones et al., 2022; Kemp et al., 2006) and Andes ($n = 566$) (Hervé et al., 2014, Hervé et al., 2013; Pankhurst et al., 2016; Rapela et al., 2021) with 10th percentile contours shown. They are compared to zircon and whole-rock εHf versus $\delta^{18}O$ for whole-rock, quartz, and zircon from the Samail MHG. Results of three end-member (basalt, Fe-Mn precipitates, metapelites) mixing calculations are also shown with ticks along the curves representing 10 % mixing increments. The mantle field is based on mantle-like zircon (Valley et al., 2005) and depleted mantle evolution line. Average metapelite is from Hopkinson et al. (2017). The O and Hf of Fe-Mn sediments are based on Knaack et al. (2023) and references therein. Average pelagic sediment and chert are shown for comparison (Chauvel et al., 2009; Valley et al., 2005; Vervoort et al., 2011). See Table SM2a for compiled data.

Spencer et al. (2017) constrained the sedimentary source of the MHG using zircon $\delta^{18}O$ data suggesting the contribution of high-$\delta^{18}O$ sediments such as shale and chert. However, while previous models suggested that chert might undergo total fusion within finely laminated shale layers (Spencer et al., 2017), the high melting point of silica presents a thermodynamic challenge. Under typical subduction zone conditions, silica would require substantial heat to melt, making it less likely to contribute to melt formation compared to other sedimentary components. Fe-Mn sediments have significantly lower melting points when compared to silica (chert) and would begin to melt at much lower temperatures. The presence of volatile-rich fluids in subduction zones could further lower the melting points of these components (e.g., Bang et al., 2024; Hacker, 2008). This suggests that Fe-Mn sediments and associated clay minerals make them suitable compositions. Thus, given the widespread distribution of Fe-Mn sediments on the ocean floor, their wide range of $\delta^{18}O$ (up to 29.5 ‰), and their Hf values (Fig. 5C and 7), Fe-Mn sediments could also be considered a source for the formation of the MHG. The $\delta^{18}O$ values of the MHG could reflect the partial melting of an Fe-Mn sediment composition that sits along the mixing trend of the mantle field and the highest $\delta^{18}O$ value of the Fe-Mn sediments in the plot of Hf and O (Fig. 7).

Furthermore, Nd-Hf decoupling observed in the Samail MHG samples (Fig. 2D) is consistent with the contribution of the Fe-Mn sediments in the source. The negative εNd values reflect a 'crustal signature' from the melted metasediments on top of the subducted oceanic crust. However, the positive εHf values could reflect a zircon-rich metasedimentary protolith ("zircon effect"), where residual zircon survived during metasediment melting during oceanic crust subduction, retaining a significant amount of ^{176}Hf at the source. Another possibility is that the pelagic clays in the marine sediments that contributed to the formation of the Samail MHG were dominated by Fe-Mn oxyhydroxides (or hydrogenetic sediments; see also work from [Pang et al. (2021)]. These sediments are precipitated from sea-water and hydrothermal fluids, also including authigenic clays and biogenic phosphates, all of which may scavenge, adsorb, or co-precipitate REE and Hf (Vervoort et al., 2011). These clays would have high radiogenic Hf and less radiogenic Nd, indicating that the Hf-Nd budget was controlled by Fe-Mn oxyhydroxide-bearing clays with radiogenic Hf isotopes relative to Nd.

In summary, Fe-Mn precipitates exhibit isotopes and trace element data that align well with those required for the genesis of the MHG. This would require the paleo-continental shelf of the Samail ophiolite to host Fe-Mn precipitates and pelagic pelitic mud, suggesting a more complex depositional environment than previously suspected. The coexistence of these components could provide further insights into the geochemical processes and sources contributing to the formation of these unique granitoids, as well as other S-types.

Despite these insights, our dataset has limitations in capturing the full isotopic variability across the ophiolite. While this study provides new isotopic constraints on the petrogenesis of MHG, some of our coupled isotopic datasets, where multiple isotopic systems were analyzed on the same samples, are primarily derived from the northern portion of the ophiolite. As a result, our interpretations involving Hf and O isotopes are most applicable to granitoids from this region and may not fully capture the geographic and temporal variations observed across the entire ophiolite belt.

5.3. *Fe-Mn sedimentary source and tectonic setting constrained by Li and H isotopes in muscovite*

The $\delta^{7}Li$ values from the Samail MHG, ranging from 13.9 to 34.1 ‰ are anomalously high when compared to other granitoid rocks of similar composition (Fig. 8), such as Li-rich pegmatites from the Jiajika province in China [−3.5 to 11.6 ‰; (Liu et al., 2017; Zhang et al., 2021)] and Harney Peak granites and pegmatites in the United States [−2.6 to 11.4 ‰; (Barnes et al., 2012; Teng et al., 2006)]. Ternary diagram in figure SM6 (Ballouard et al., 2016) shows muscovite from analyzed MHG samples plotted mostly within the zone of primary muscovite.

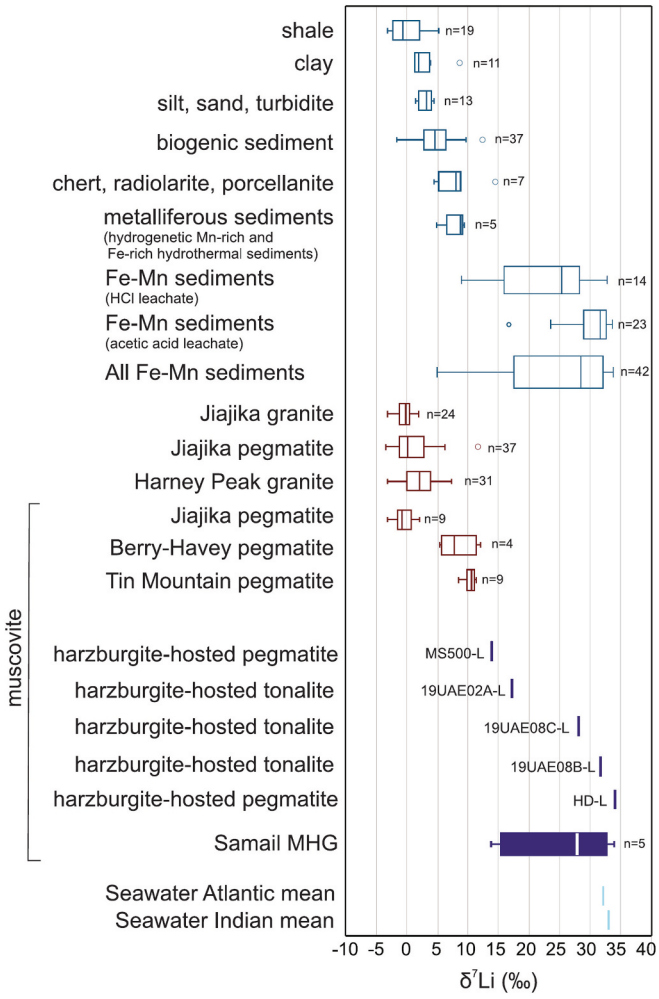

Fig. 8. Distribution of $\delta^{7}Li$ of marine sediments, granitoids, and seawater based on data from this study and previous work (Chan et al., 2006; Hall et al., 2005; Steinhoefel et al., 2021; Teng et al., 2006; Teng et al., 2004; Zhang et al., 2021). Circles are outliers. See the compilation for lithium isotopes in Table SM2g.

Chan et al. (2006) showed that Fe-Mn sediments (oxyhydroxides) from the Tonga Trench have $\delta^{7}Li$ values ranging from 6 to 10 ‰ (metalliferous sediments from Fig. 8) and that they may adsorb Li from seawater or saline porewaters, which typically have high $\delta^{7}Li$ ranging from 20 to 32 ‰ (Chan et al., 2006; James and Palmer, 2000; Lui-Heung and Edmond, 1988; Moriguti and Nakamura, 1998; Tang et al., 2007; Tomascak et al., 1999; You and Chan, 1996). Seawater-like compositions have been observed for ferromanganese crusts (Fig. SM6), with a $\delta^{7}Li$ of ~31 ‰ [global sweater mean; (James and Palmer, 2000; Tang et al., 2007; Tomascak et al., 1999)]. The adsorption of Li onto the outsides of the clay minerals and slow incorporation into the structural sites of clays may be a possible mechanism of heavy Li enrichment of Fe-Mn sediments (Anderson et al., 1989). Thus, slowly accumulating sediments may acquire Li from seawater, resulting in relatively high $\delta^{7}Li$ values.

During partial melting of sediments on top of the underthrusting slab during subduction, ^{6}Li is selectively retained in minerals whereas coexisting fluids are relatively enriched in ^{7}Li (Chan et al., 2002; Chan et al., 1993). Alpine eclogites with isotopically light Li signatures provide evidence of this isotopic fractionation process (Zack et al., 2003). Haase et al. (2015) suggest metasedimentary melts that contribute to the genesis of the Samail MHG formed from the subducting plate beneath the Samail ophiolite intruded cold shallow part and hotter interior of the

mantle wedge. They argue the MHG were emplaced in the shallow mantle and must have been relatively cold, because it did not react with the felsic melts and intrusive boundaries are sharp. Close to the trench, the mantle wedge consists of serpentinite with temperatures <800° (Hyndman and Peacock, 2003). Lower temperature subduction results in higher isotope fractionation due to the exsolution of high δ^7Li fluids during partial melting of metasediments, in agreement with the proposed source and tectonic model. This model is also supported by the δ^2H values obtained from muscovite, which indicate the source of fluids that contributed to tshe formation of the MHG was most likely metamorphic waters (Fig. SM7) when compared to other water types. δ^2H values of the analyzed muscovite from the MHG range from −47 to −14 ‰ with a median of −37 ‰. Four out of the seven analyzed samples yield δ^{18}O values of whole-rock, quartz or zircon >16 ‰, supporting the idea that the Samail MHG formed from the subducting plate beneath the ophiolite and associated hydrous metasedimentary melts, with no interaction with other water sources during petrogenesis. However, it is important to note that the Li and H isotope data presented in this study are derived from samples from the northern portion of the ophiolite belt. While these results offer valuable insights, they may not fully reflect the isotopic variability across the entire ophiolite belt.

6. Conclusions

Negative εNd and slightly positive εHf values suggest the involvement of ancient sedimentary sources in the formation of the Samail mantle-hosted granitoids. Oxygen isotopes from zircon, quartz and whole-rock are remarkably variable, implying a potential mixture of altered mafic and sedimentary sources, also demonstrated by Sr and Pb isotopic signatures. Using a recently proposed discrimination tool based on Ce-U-Th concentrations and Hf-O isotopes, we argue that Fe-Mn sediments (i.e., hydrothermal and hydrogenetic), together with pelagic mud, might have contributed to the formation of the Samail mantle-hosted granitoids. This model is supported by enriched δ^7Li values in muscovite from the MHG, similar to those found in Fe-Mn sediments. These findings have broader implications for models of mantle heterogeneity over time because the Samail mantle-hosted granitoids, derived from metasedimentary sources, may represent crustal components transported to the upper mantle from a complex deep-sea depositional environment.

CRediT authorship contribution statement

Tiago Valim Angelo: Writing – review & editing, Writing – original draft, Visualization, Validation, Software, Project administration, Methodology, Investigation, Funding acquisition, Formal analysis, Conceptualization. **Christopher J. Spencer:** Writing – review & editing, Supervision, Project administration, Methodology, Investigation, Funding acquisition, Conceptualization. **Hong-Yan Li:** Writing – review & editing, Validation, Methodology, Investigation, Funding acquisition. **Derek Knaack:** Writing – review & editing, Validation, Methodology, Investigation. **Ziyi Zhu:** Writing – review & editing, Visualization, Validation, Methodology, Investigation. **Marina Seraine:** Writing – review & editing, Validation, Methodology, Investigation. **Nick M.W. Roberts:** Writing – review & editing, Visualization, Validation, Investigation. **Evelyne Leduc:** Writing – review & editing, Validation, Methodology, Investigation. **Sophie Divilek:** Writing – review & editing, Methodology, Investigation. **Anna Ren:** Writing – review & editing, Methodology, Investigation. **Brian Joy:** Investigation, Methodology, Writing – review & editing. **Gui-Mei Lu:** Writing – review & editing, Validation, Investigation.

Declaration of competing interest

The authors declare that they have no known competing financial interests or personal relationships that could have appeared to influence the work reported in this paper.

Acknowledgements

Part of this research was financially supported by the National Natural Science Foundation of China (NFSC Project 42425304) from Li, H. Y. This work is part of PhD thesis project conducted at Queen's University by T.V.A.

Appendix A. Supplementary data

Supplementary data to this article can be found online at https://doi.org/10.1016/j.chemgeo.2025.122759.

Data availability

Data are available through figshare at https://doi.org/10.6084/m9.figshare.28055894.v6

References

Adachi, Y., Miyashita, S., 2003. Geology and petrology of the plutonic complexes in the Wadi Fizh area: Multiple magmatic events and segment structure in the northern Oman ophiolite. Geochem. Geophys. Geosyst. 4, 8619. https://doi.org/10.1029/2001GC000272.

Al Humadi, H., Väisänen, M., Ismail, S.A., Lehtonen, M., Johanson, B., 2021. Subducted basalts and sediments as sources for felsic dykes in the mawat ophiolite, NE Iraq. Ofioliti 46, 27–41. https://doi.org/10.4454/ofioliti.v46i1.536.

Albarède, F., Simonetti, A., Vervoort, J.D., Blichert-Toft, J., Abouchami, W., 1998. A Hf-Nd isotopic correlation in ferromanganese nodules. Geophys. Res. Lett. 25, 3895–3898. https://doi.org/10.1029/1998GL900008.

Alberts, R.C., 2016. Petrogenesis of Plagiogranite and Granitoid in the Oman Ophiolite: A Comparative Study Using Oxygen Isotopes and Trace Elements in Zircon. Master's Thesis.. Ohio University.

Amri, I., Benoit, M., Ceuleneer, G., 1996. Tectonic setting for the genesis of oceanic plagiogranites: evidence from a paleo-spreading structure in the Oman ophiolite. Earth Planet. Sci. Lett. 139, 177–194. https://doi.org/10.1016/0012-821x(95)00233-3.

Amri, I., Ceuleneer, G., Benoit, M., Python, M., Puga, E., Targuisti, K., 2007. Genesis of granitoids by interaction between mantle peridotites an hydrothermal fluids in oceanic spreading setting in the Oman Ophiolite. Geogaceta 23–26.

Anderson, M.A., Bertsch, P.M., Miller, W.P., 1989. Exchange and apparent fixation of lithium in selected soils and clay minerals. Soil Sci. 148.

Angelo, T.V., Spencer, C.J., Cavosie, A.J., Thomas, R., Li, H.-Y., 2023. Petrogenesis of Mantle-Hosted Granitoids from the Samail Ophiolite. J. Petrol. 64, egad021. https://doi.org/10.1093/petrology/egad021.

Bailey, E.H., 1981. Geologic map of Muscat-Ibra area. Sultanate Oman J. Geophys. Res. 86, 2495–2782.

Baker, J., Peate, D., Waight, T., Meyzen, C., 2004. Pb isotopic analysis of standards and samples using a 207Pb–204Pb double spike and thallium to correct for mass bias with a double-focusing MC-ICP-MS. Chem. Geol. 211, 275–303.

Ballouard, C., Poujol, M., Boulvais, P., Branquet, Y., Tartèse, R., Vigneresse, J.-L., 2016. Nb-Ta fractionation in peraluminous granites: a marker of the magmatic-hydrothermal transition. Geology 44, 231–234. https://doi.org/10.1130/G37475.1.

Bang, Y., Hwang, H., Liermann, H.-P., Kim, D.Y., He, Y., Jeon, T.-Y., Shin, T.J., Zhang, D., Popov, D., Lee, Y., 2024. A role for subducting clays in the water transportation into the Earth's lower mantle. Nat. Commun. 15, 4428. https://doi.org/10.1038/s41467-024-48501-z.

Barnes, E.M., Weis, D., Groat, L.A., 2012. Significant Li isotope fractionation in geochemically evolved rare element-bearing pegmatites from the Little Nahanni Pegmatite Group, NWT, Canada. Lithos 132–133, 21–36. https://doi.org/10.1016/j.lithos.2011.11.014.

Bayon, G., Skonieczny, C., Delvigne, C., Toucanne, S., Bermell, S., Ponzevera, E., André, L., 2016. Environmental Hf–Nd isotopic decoupling in World river clays. Earth Planet. Sci. Lett. 438, 25–36. https://doi.org/10.1016/j.epsl.2016.01.010.

Black, L.P., Kamo, S.L., Allen, C.M., Davis, D.W., Aleinikoff, J.N., Valley, J.W., Mundil, R., Campbell, I.H., Korsch, R.J., Williams, I.S., Foudoulis, C., 2004. Improved 206Pb/238U microprobe geochronology by the monitoring of a trace-element-related matrix effect; SHRIMP, ID-TIMS, ELA-ICP-MS and oxygen isotope documentation for a series of zircon standards. Chem. Geol. 205, 115–140. https://doi.org/10.1016/j.chemgeo.2004.01.003.

Bonin, B., Janoušek, V., Moyen, J.-F., 2020. Chemical variation, modal composition and classification of granitoids. Geol. Soc. London, Spec. Publ. 491, 9 LP – 51. doi: https://doi.org/10.1144/SP491-2019-138.

Boudier, F., Ceuleneer, G., Nicolas, A., 1988. Shear zones, thrusts and related magmatism in the Oman ophiolite: initiation of thrusting on an oceanic ridge. Tectonophysics 151, 275–296.

Briqueu, L., Mével, C., Boudier, F., 1991. Sr, Nd and Pb isotopic constraints in the genesis of a calc-alkaline plutonic suite in Oman ophiolite related to the obduction process.

In: Ophiolite Genesis and Evolution of the Oceanic Lithosphere. Springer, pp. 517–542.
Browning, P., Smewing, J.D., 1981. Processes in magma chambers beneath spreading axes: evidence from magmatic associations in the Oman Ophiolite. J. Geol. Soc. Lond. 138, 279–280.
Chan, L.-H., Edmond, J.M., Thompson, G., 1993. A lithium isotope study of hot springs and metabasalts from Mid-Ocean Ridge Hydrothermal Systems. J. Geophys. Res. Solid Earth 98, 9653–9659. https://doi.org/10.1029/92JB00840.
Chan, L.-H., Alt, J.C., Teagle, D.A.H., 2002. Lithium and lithium isotope profiles through the upper oceanic crust: a study of seawater–basalt exchange at ODP Sites 504B and 896A. Earth Planet. Sci. Lett. 201, 187–201. https://doi.org/10.1016/S0012-821X(02)00707-0.
Chan, L.-H., Leeman, W.P., Plank, T., 2006. Lithium isotopic composition of marine sediments. Geochem. Geophys. Geosyst. 7. https://doi.org/10.1029/2005GC001202.
Chappell, B., White, A., 1974. Two contrasting granite types. Pacific Geol. 8, 173–174.
Chauvel, C., Marini, J.-C., Plank, T., Ludden, J.N., 2009. Hf-Nd input flux in the Izu-Mariana subduction zone and recycling of subducted material in the mantle. Geochem. Geophys. Geosyst. 10. https://doi.org/10.1029/2008GC002101.
Chen, J.H., Pallister, J.S., 1981. Lead isotopic studies of the Samail Ophiolite. Oman. J. Geophys. Res. Solid Earth 86, 2699–2708. https://doi.org/10.1029/JB086iB04p02699.
Class, C., Lehnert, K., 2012. PetDB expert MORB (mid-ocean ridge basalt) compilation. EarthChem Libr. 1–2.
Cox, J., Searle, M., Pedersen, R., 1999. The petrogenesis of leucogranitic dykes intruding the northern Semail ophiolite, United Arab Emirates: Field relationships, geochemistry and Sr/Nd isotope systematics. Contrib. Mineral. Petrol. 137, 267–287. https://doi.org/10.1007/s004100050550.
de Graaff, S.J., Goodenough, K.M., Klaver, M., Lissenberg, C.J., Jansen, M.N., Millar, I., Davies, G.R., 2019. Evidence for a Moist to Wet Source transition throughout the Oman-UAE Ophiolite, and Implications for the Geodynamic history. Geochem. Geophys. Geosystems 20, 651–672. https://doi.org/10.1029/2018GC007923.
Dhuime, B., Hawkesworth, C., Cawood, P., 2011. When continents formed. Science 80-.). 331, 154–155.
Dhuime, B., Hawkesworth, C.J., Cawood, P.A., Storey, C.D., 2012. A Change in the Geodynamics of Continental Growth 3 billion years Ago. Science 80-.). 335, 1334–1336. https://doi.org/10.1126/science.1216066.
Dilek, Y., Furnes, H., 2009. Structure and geochemistry of Tethyan ophiolites and their petrogenesis in subduction rollback systems. Lithos 113, 1–20.
Fisher, C.M., Vervoort, J.D., Hanchar, J.M., 2014. Guidelines for reporting zircon Hf isotopic data by LA-MC-ICPMS and potential pitfalls in the interpretation of these data. Chem. Geol. 363, 125–133. https://doi.org/10.1016/j.chemgeo.2013.10.019.
France, L., Ildefonse, B., Koepke, J., 2009. Interactions between magma and hydrothermal system in Oman ophiolite and in IODP Hole 1256D: Fossilization of a dynamic melt lens at fast spreading ridges. Geochem. Geophys. Geosyst. 10. https://doi.org/10.1029/2009GC002652.
Freund, S., Haase, K.M., Keith, M., Beier, C., Garbe-Schönberg, D., 2014. Constraints on the formation of geochemically variable plagiogranite intrusions in the Troodos Ophiolite. Cyprus. Contrib. to Mineral. Petrol. 167, 978. https://doi.org/10.1007/s00410-014-0978-6.
Glennie, K.W., Boeuf, M.G.A., Clarke, M.W.H., Moody-Stuart, M., Pilaar, W.F.H., Reinhardt, B.M., 1973. Late cretaceous nappes in Oman Mountains and their geologic evolution. Am. Assoc. Pet. Geol. Bull. 57, 5–27.
Glennie, K.W.K., Boeuf, M., Clarke, M., Moody Stuart, M., Pilaar, W., Reinhardt, B., 1974. Geology of the Oman Mountains. Geol. Oman Mount. 31, 423.
Goodenough, K.M., Styles, M.T., Schofield, D., Thomas, R.J., Crowley, Q.C., Lilly, R.M., McKervey, J., Stephenson, D., Carney, J.N., 2010. Architecture of the Oman-UAE ophiolite: evidence for a multi-phase magmatic history. Arab. J. Geosci. 3, 439–458. https://doi.org/10.1007/s12517-010-0177-3.
Goodenough, K.M., Thomas, R.J., Styles, M.T., Schofield, D.I., MacLeod, C.J., 2014. Records of ocean growth and destruction in the Oman–UAE ophiolite. Elements 10, 109–114.
Grantham, G.H., Goedhart, M.L., Wipplinger, P.E., Thomas, R.J., Eglington, B.M., Harmer, R.E., Hartzer, F.J., 2003. The Surface Geology of the Emirate of Fujairah. Unpubl. Report. Dep. Ind. Econ. Gov, Fujairah, United Arab Emirates.
Gregory, R.T., Taylor Jr., H.P., Taylor Jr., H.P., 1981. An oxygen isotope profile in a section of cretaceous oceanic crust, Samail Ophiolite, Oman: evidence for δ18O buffering of the oceans by deep (> 5 km) seawater-hydrothermal circulation at mid-ocean ridges. J. Geophys. Res. Solid Earth 86, 2737–2755. https://doi.org/10.1029/JB086iB04p02737.
Grimes, C.B., Ushikubo, T., Kozdon, R., Valley, J.W., 2013. Perspectives on the origin of plagiogranite in ophiolites from oxygen isotopes in zircon. Lithos 179, 48–66. https://doi.org/10.1016/j.lithos.2013.07.026.
Haase, K.M., Freund, S., Koepke, J., Hauff, F., Erdmann, M., 2015. Melts of sediments in the mantle wedge of the Oman ophiolite. Geology 43, 275–278. https://doi.org/10.1130/G36451.1.
Haase, K.M., Freund, S., Beier, C., Koepke, J., Erdmann, M., Hauff, F., 2016. Constraints on the magmatic evolution of the oceanic crust from plagiogranite intrusions in the Oman ophiolite. Contrib. Mineral. Petrol. 171, 1–16. https://doi.org/10.1007/s00410-016-1261-9.
Hacker, B.R., 2008. H2O subduction beyond arcs. Geochem. Geophys. Geosyst. 9. https://doi.org/10.1029/2007GC001707.
Hall, J.M., Chan, L.-H., McDonough, W.F., Turekian, K.K., 2005. Determination of the lithium isotopic composition of planktic foraminifera and its application as a paleo-seawater proxy. Mar. Geol. 217, 255–265. https://doi.org/10.1016/j.margeo.2004.11.015.
Hauff, F., Hoernle, K., Schmidt, A., 2003. Sr-Nd-Pb composition of Mesozoic Pacific oceanic crust (Site 1149 and 801, ODP Leg 185): Implications for alteration of ocean crust and the input into the Izu-Bonin-Mariana subduction system. Geochem. Geophys. Geosyst. 4. https://doi.org/10.1029/2002GC000421.
Hawkins, J.W., 2003. Geology of supra-subduction zones-Implications for the origin of ophiolites. In: Newcomb, S. (Ed.), Dilek, Y. Ophiolite Concept and the Evolution of Geological Thought, Geological Society of America, pp. 227–268. https://doi.org/10.1130/0-8137-2373-6.227.
Heinrich, K.F.J., 1987. Mass absorption coefficients for electron probe microanalysis. Proc. 11th Int. Congr. X-Ray Opt. Microanal. 67–119.
Hervé, F., Calderón, M., Fanning, C.M., Pankhurst, R.J., Godoy, E., 2013. Provenance variations in the late Paleozoic accretionary complex of Central Chile as indicated by detrital zircons. Gondwana Res. 23, 1122–1135. https://doi.org/10.1016/j.gr.2012.06.016.
Hervé, F., Fanning, C.M., Calderón, M., Mpodozis, C., 2014. Early Permian to Late Triassic batholiths of the Chilean Frontal Cordillera (28°–31°S): SHRIMP U–Pb zircon ages and Lu–Hf and O isotope systematics. Lithos 184–187, 436–446. doi: https://doi.org/10.1016/j.lithos.2013.10.018.
Hopkinson, T.N., 2016. Geochemical Insights into Crustal Melting in the Bhutan Himalaya.
Hopkinson, T.N., Harris, N.B.W., Warren, C.J., Spencer, C.J., Roberts, N.M.W., Horstwood, M.S.A., Parrish, R.R., EIMF, 2017. The identification and significance of pure sediment-derived granites. Earth Planet. Sci. Lett. 467, 57–63. https://doi.org/10.1016/j.epsl.2017.03.018.
Hyndman, R.D., Peacock, S.M., 2003. Serpentinization of the forearc mantle. Earth Planet. Sci. Lett. 212, 417–432. https://doi.org/10.1016/S0012-821X(03)00263-2.
James, R.H., Palmer, M.R., 2000. The lithium isotope composition of international rock standards. Chem. Geol. 166, 319–326. https://doi.org/10.1016/S0009-2541(99)00217-X.
Jeon, H., Williams, I.S., 2018. Trace inheritance—Clarifying the zircon O-Hf isotopic fingerprint of I-type granite sources: Implications for the restite model. Chem. Geol. 476, 456–468. https://doi.org/10.1016/j.chemgeo.2017.11.041.
Jochum, K.P., Weis, U., Stoll, B., Kuzmin, D., Yang, Q., Raczek, I., Jacob, D.E., Stracke, A., Birbaum, K., Frick, D.A., Günther, D., Enzweiler, J., 2011. Determination of Reference Values for NIST SRM 610–617 Glasses following ISO guidelines. Geostand. Geoanal. Res. 35, 397–429. https://doi.org/10.1111/j.1751-908X.2011.00120.x.
Jones, C.L., Orovan, E.A., Meffre, S., Thompson, J., Belousova, E.A., Cracknell, M.J., Everard, J., Bottrill, R., Bodorkos, S., Cooke, D.R., 2022. Zircon O and Lu-Hf isotope evidence of mantle and supracrustal origins of Tasmanian Devonian granites. Gondwana Res. 110, 1–12. https://doi.org/10.1016/j.gr.2022.06.004.
Joun, H., Kokkalas, S., Tombros, S., 2019. Recycled oceanic crust as a source for tonalite intrusions in the mantle section of the Khor Fakkan block, Semail ophiolite (UAE). Geosci. Front. 10, 1187–1210. https://doi.org/10.1016/j.gsf.2018.09.006.
Kemp, A.I.S., Hawkesworth, C.J., Paterson, B.A., Kinny, P.D., 2006. Episodic growth of the Gondwana supercontinent from hafnium and oxygen isotopes in zircon. Nature 439, 580–583. https://doi.org/10.1038/nature04505.
Kemp, A.I.S., Hawkesworth, C.J., Foster, G.L., Paterson, B.A., Woodhead, J.D., Hergt, J.M., Gray, C.M., Whitehouse, M.J., 2007. Magmatic and Crustal Differentiation history of Granitic Rocks from Hf-O Isotopes in Zircon. Science (80-.) 315, 980–983. https://doi.org/10.1126/science.1136154.
Kim, S.S.W., Jang, Y., Kwon, S., Samuel, V.O., Kim, S.S.W., Park, S.I., Santosh, M., Kokkalas, S., 2020. Petro-tectonic evolution of metamorphic sole of the Semail ophiolite. UAE. Gondwana Res. 86, 203–221. https://doi.org/10.1016/j.gr.2020.05.013.
Kimura, J.-I., Gill, J.B., van Keken, P.E., Kawabata, H., Skora, S., 2017. Origin of geochemical mantle components: Role of spreading ridges and thermal evolution of mantle. Geochem. Geophys. Geosyst. 18, 697–734. https://doi.org/10.1002/2016GC006696.
Knaack, D.R., Leybourne, M.I., Layton-Matthews, D., Hein, J.R., Stern, R.J., Wysoczanski, R., Faure, K., Usui, A., Al, T., McDonald, A., Dobosz, A., Pufahl, P., 2023. The role of depositional environment and chemical composition on the triple oxygen isotope ratios of ferromanganese precipitates and their endmember components. Chem. Geol. 642, 121785. https://doi.org/10.1016/j.chemgeo.2023.121785.
Koepke, J., Feig, S.T., Snow, J., Freise, M., 2004. Petrogenesis of oceanic plagiogranites by partial melting of gabbros: an experimental study. Contrib. Mineral. Petrol. 146, 414–432. https://doi.org/10.1007/s00410-003-0511-9.
Koepke, J., Berndt, J., Feig, S.T., Holtz, F., 2007. The formation of SiO2-rich melts within the deep oceanic crust by hydrous partial melting of gabbros. Contrib. Mineral. Petrol. 153, 67–84. https://doi.org/10.1007/s00410-006-0135-y.
Li, X.-H., Long, W.-G., Li, Q.-L., Liu, Y., Zheng, Y.-F., Yang, Y.-H., Chamberlain, K.R., Wan, D.-F., Guo, C.-H., Wang, X.-C., Tao, H., 2010. Penglai Zircon Megacrysts: A Potential New Working Reference Material for Microbeam Determination of Hf–O Isotopes and U–Pb Age. Geostand. Geoanal. Res. 34, 117–134. doi:https://doi.org/10.1111/j.1751-908X.2010.00036.x.
Li, C.-F., Li, X.-H.X.-H., Li, Q.-L., Guo, J.-H., Li, X.-H.X.-H., Yang, Y.-H., 2012. Rapid and precise determination of Sr and Nd isotopic ratios in geological samples from the same filament loading by thermal ionization mass spectrometry employing a single-step separation scheme. Anal. Chim. Acta 727, 54–60.
Li, J., Tang, S., Zhu, X., Pan, C., 2017. Production and certification of the reference material GSB 04-3258-2015 as a 143Nd/144Nd isotope ratio reference. Geostand. Geoanal. Res. 41, 255–262.
Li, W., Liu, X.-M., Godfrey, L.V., 2019. Optimisation of Lithium Chromatography for Isotopic Analysis in Geological Reference Materials by MC-ICP-MS. Geostand. Geoanal. Res. 43, 261–276. https://doi.org/10.1111/ggr.12254.

Liebmann, J., Kirkland, C.L., Cliff, J.B., Spencer, C.J., Cavosie, A.J., 2023. Strategies towards robust interpretations of in situ zircon oxygen isotopes. Geosci. Front. 14, 101523. https://doi.org/10.1016/j.gsf.2022.101523.
Liew, T.C., Hofmann, A.W., 1988. Precambrian crustal components, plutonic associations, plate environment of the Hercynian Fold Belt of Central Europe: indications from a Nd and Sr isotopic study. Contrib. Mineral. Petrol. 98, 129–138.
Lippard, S.J., Shelton, A.W., Gass, I.G., 1986. The ophiolite of northern Oman. Geol. Soc. Lond. Mem. 11, 178.
Liu, L.J., Wang, D.H., Hou, K.J., Tian, S.H., Zhao, Y., Fu, X.F., Yuan, L.P., Hao, X.F., 2017. Application of lithium isotope to Jiajika new no. 3 pegmatite lithium polymetallic vein in Sichuan. Earth Sci. Front. 24, 167–171.
Lui-Heung, C., Edmond, J.M., 1988. Variation of lithium isotope composition in the marine environment: a preliminary report. Geochim. Cosmochim. Acta 52, 1711–1717. https://doi.org/10.1016/0016-7037(88)90239-6.
Martin, L.A.J., Duchêne, S., Deloule, E., Vanderhaeghe, O., 2008. Mobility of trace elements and oxygen in zircon during metamorphism: Consequences for geochemical tracing. Earth Planet. Sci. Lett. 267, 161–174. https://doi.org/10.1016/j.epsl.2007.11.029.
McCulloch, M.T., Gregory, R.T., Wasserburg, G.J., Taylor, H.P., 1980. A neodymium, strontium, and oxygen isotopic study of the cretaceous Samail ophiolite and implications for the petrogenesis and seawater-hydrothermal alteration of oceanic crust. Earth Planet. Sci. Lett. 46, 201–211. https://doi.org/10.1016/0012-821X(80)90006-0.
Moriguti, T., Nakamura, E., 1998. High-yield lithium separation and the precise isotopic analysis for natural rock and aqueous samples. Chem. Geol. 145, 91–104. https://doi.org/10.1016/S0009-2541(97)00163-0.
Nadeau, O., Mick, E., Robidoux, P., Grassa, F., Brusca, L., Voinot, A., Leybourne, M.I., 2021. Lithium isotopes and Cu-au concentrations in hydrothermal alterations from Solfatara Volcano, Campi Flegrei caldera complex, and La Fossa volcano, Vulcano Island, Italy: Insights into epithermal ore forming environments. Ore Geol. Rev. 130, 103934. https://doi.org/10.1016/j.oregeorev.2020.103934.
Nicolas, A., Boudier, F., Ildefonse, B., 1996. Variable crustal thickness in the Oman ophiolite: Implication for oceanic crust. J. Geophys. Res. Solid Earth 101, 17941–17950. https://doi.org/10.1029/96JB00195.
Nicolas, A., Bouldier, F., Ildefonse, B., Ball, E., 2000. Accretion of Oman and United Arab Emirates ophiolite - Discussion of a new structural map. Mar. Geophys. Res. 21, 147–180. https://doi.org/10.1023/A:1026769727917.
Pang, C.-J., Tian, L., Wang, X.-C., Zhang, H., Wen, S.-N., Krapež, B., Liu, W.-J., Liu, Z.-X., Wu, T., 2021. Decoupling of Hf-Nd Isotopes in Challenger Deep Sediments, Mariana Trench: Implications for Sedimentary Hf and Nd Recycling in Subduction zones. J. Geophys. Res. Solid Earth 126. https://doi.org/10.1029/2021JB021641 e2021JB021641.
Pankhurst, R.J., Hervé, F., Fanning, C.M., Calderón, M., Niemeyer, H., Griem-Klee, S., Soto, F., 2016. The pre-Mesozoic rocks of northern Chile: U–Pb ages, and Hf and O isotopes. Earth-Science Rev. 152, 88–105. doi:https://doi.org/10.1016/j.earscirev.2015.11.009.
Payne, J.L., Hand, M., Pearson, N.J., Barovich, K.M., McInerney, D.J., 2015. Crustal thickening and clay: Controls on O isotope variation in global magmatism and siliciclastic sedimentary rocks. Earth Planet. Sci. Lett. 412, 70–76. https://doi.org/10.1016/j.epsl.2014.12.037.
Pearce, J.A., Alabaster, T., Shelton, A.W., Searle, M.P., Vine, F.J., Smith, A.G., 1981. The Oman ophiolite as a cretaceous arc-basin complex: evidence and implications. Philos. Trans. R. Soc. London. Ser. A Math. Phys. Sci. 300, 299–317. https://doi.org/10.1098/rsta.1981.0066.
Pearce, J.A., Stern, R.J., Bloomer, S.H., Fryer, P., 2005. Geochemical mapping of the Mariana arc-basin system: Implications for the nature and distribution of subduction components. Geochem. Geophys. Geosyst. 6. https://doi.org/10.1029/2004GC000895.
Peters, T., Kamber, B.S., 1994. Peraluminous potassium-rich granitoids in the Semail Ophiolite. Contrib. Mineral. Petrol. 118, 229–238. https://doi.org/10.1007/BF00306644.
Plank, T., 2014. The Chemical Composition of Subducting Sediments. Treatise Geochemistry Second Ed. 4, 607–629. https://doi.org/10.1016/B978-0-08-095975-7.00319-3.
Pouchou, J.-L., Pichoir, F., 1991. Quantitative analysis of homogeneous or stratified microvolumes applying the model "PAP,". In: Electron Probe Quantitation. Springer, pp. 31–75.
Qi, H., Coplen, T.B., Gehre, M., Vennemann, T.W., Brand, W.A., Geilmann, H., Olack, G., Bindeman, I.N., Palandri, J., Huang, L., Longstaffe, F.J., 2017. New biotite and muscovite isotopic reference materials, USGS57 and USGS58, for δ2H measurements–a replacement for NBS 30. Chem. Geol. 467, 89–99. https://doi.org/10.1016/j.chemgeo.2017.07.027.
Rapela, C.W., Hervé, F., Pankhurst, R.J., Calderón, M., Fanning, C.M., Quezada, P., Poblete, F., Palape, C., Reyes, T., 2021. The Devonian accretionary orogen of the North Patagonian cordillera. Gondwana Res. 96, 1–21. https://doi.org/10.1016/j.gr.2021.04.004.
Reed, S.J.B., 1990. Fluorescence effects in quantitative microprobe analysis. Microbeam Anal. 109–114.
Rioux, M., Bowring, S., Kelemen, P., Gordon, S., Dudás, F., Miller, R., 2012. Rapid crustal accretion and magma assimilation in the Oman-U.A.E. Ophiolite: High precision U-Pb zircon geochronology of the gabbroic crust. J. Geophys. Res. Solid Earth 117, 1–12. https://doi.org/10.1029/2012JB009273.
Rioux, M., Bowring, S., Kelemen, P., Gordon, S., Miller, R., Dudás, F., 2013. Tectonic development of the Samail ophiolite: High-precision U-Pb zircon geochronology and Sm-Nd isotopic constraints on crustal growth and emplacement. J. Geophys. Res. Solid Earth 118, 2085–2101. https://doi.org/10.1002/jgrb.50139.
Rioux, M., Benoit, M., Amri, I., Ceuleneer, G., Garber, J.M., Searle, M., Leal, K., 2021a. The origin of felsic intrusions within the mantle section of the Samail ophiolite: Geochemical evidence for three distinct mixing and fractionation trends. J. Geophys. Res. Solid Earth n/a e2020JB020760. https://doi.org/10.1029/2020JB020760.
Rioux, M., Garber, J.M., Searle, M., Kelemen, P., Miyashita, S., Adachi, Y., Bowring, S., 2021b. High-precision U-Pb zircon dating of late magmatism in the Samail ophiolite: a record of subduction initiation. J. Geophys. Res. Solid Earth n/a e2020JB020758. https://doi.org/10.1029/2020JB020758.
Roberts, N.M.W., Yakymchuk, C., Spencer, C.J., Keller, C.B., Tapster, S.R., 2024. Revisiting the discrimination and distribution of S-type granites from zircon trace element composition. Earth Planet. Sci. Lett. 633, 118638. https://doi.org/10.1016/j.epsl.2024.118638.
Rollinson, H., 2009. New models for the genesis of plagiogranites in the Oman ophiolite. Lithos 112, 603–614. https://doi.org/10.1016/j.lithos.2009.06.006.
Rollinson, H., 2014. Plagiogranites from the mantle section of the Oman Ophiolite: Models for early crustal evolution. Geol. Soc. Spec. Publ. 392, 247–261. https://doi.org/10.1144/SP392.13.
Rollinson, H., 2015. Slab and sediment melting during subduction initiation: granitoid dykes from the mantle section of the Oman ophiolite. Contrib. Mineral. Petrol. 170, 1–20. https://doi.org/10.1007/s00410-015-1177-9.
Rollinson, H., Adetunji, J., 2015. The geochemistry and oxidation state of podiform chromitites from the mantle section of the Oman ophiolite: a review. Gondwana Res. 27, 543–554. https://doi.org/10.1016/j.gr.2013.07.013.
Rollinson, H.R., Searle, M.P., Abbasi, I.A., Al-Lazki, A.I., Al Kindi, M.H., 2014. Tectonic evolution of the Oman mountains: an introduction. Geol. Soc. Spec. Publ. 392, 1–7. https://doi.org/10.1144/SP392.1.
Rubatto, D., 2017. Zircon: the Metamorphic Mineral. Rev. Mineral. Geochem. 83, 261–295. https://doi.org/10.2138/rmg.2017.83.9.
Rudnick, R.L., Gao, S., 2003. 3.01 - Composition of the Continental Crust. In: Holland, H. D., Turekian, K.K.B.T.-T., on G. (Eds.), Treatise on Geochemistry, Second edition. Pergamon, Oxford, pp. 1–64. https://doi.org/10.1016/B0-08-043751-6/03016-4.
Searle, M., Cox, J., 1999. Tectonic setting, origin, and obduction of the Oman ophiolite. Bull. Geol. Soc. Am. 111, 104–122. https://doi.org/10.1130/0016-7606(1999)111<0104:TSOAOO>2.3.CO;2.
Searle, M.P., Cox, J.O.N., 2002. Subduction zone metamorphism during formation and emplacement of the Semail ophiolite in the Oman Mountains. Geol. Mag. 139, 241–255.
Searle, M.P., Malpas, J., 1980. Structure and metamorphism of rocks beneath the Semail ophiolite of Oman and their significance in ophiolite obduction. Trans. R. Soc. Edinburgh 71, 247–262. https://doi.org/10.1017/S0263593300013614.
Searle, M.P., Waters, D.J., Garber, J.M., Rioux, M., Cherry, A.G., Ambrose, T.K., 2015. Structure and metamorphism beneath the obducting Oman ophiolite: evidence from the Bani Hamid granulites, northern Oman mountains. Geosphere 11, 1812–1836. https://doi.org/10.1130/GES01199.1.
Metcalf, R. V, Shervais, J.W., 2008. Suprasubduction-zone ophiolites: Is there really an ophiolite conundrum?, in: Wright, J.E., Shervais, J.W. (Eds.), Ophiolites, Arcs, and Batholiths: A Tribute to Cliff Hopson. Geological Society of America, pp. 191–222. doi:https://doi.org/10.1130/2008.2438(07).
Spencer, C.J., Cavosie, A.J., Raub, T.D., Rollinson, H., Jeon, H., Searle, M.P., Miller, J.A., McDonald, B.J., Evans, N.J., 2017. Evidence for melting mud in Earth's mantle from extreme oxygen isotope signatures in zircon. Geology 45, 975–978. https://doi.org/10.1130/G39402.1.
Springer, G., 1967. The correction for "continuous fluorescence" in electronprobe microanalysis. Neues Jahrb. Miner. Abhandl 106, 241–256.
Springer, G., 1971. Fluorescence by the X-Ray Continuum in Multi-Element Targets: Falconbridge Nickel Mines Limited. Thornhill, Ontario, Canada, Rep (FRL-138).
Stacey, J.S.T., Kramers, J.D., 1975. Approximation of terrestrial lead isotope evolution by a two-stage model. Earth Planet. Sci. Lett. 26, 207–221.
Stakes, D.S., Taylor, H.P., 1992. The northern Samail ophiolite: an oxygen isotope, microprobe, and field study. J. Geophys. Res. Solid Earth 97, 7043–7080. https://doi.org/10.1029/91JB02743.
Stakes, D.S., Taylor, H.P., 2003. Oxygen isotope and chemical studies on the origin of large plagiogranite bodies in northern Oman, and their relationship to the overlying massive sulphide deposits. Geol. Soc. London. Spec. Publ. 218, 315–351. https://doi.org/10.1144/GSL.SP.2003.218.01.17.
Steinhoefel, G., Brantley, S.L., Fantle, M.S., 2021. Lithium isotopic fractionation during weathering and erosion of shale. Geochim. Cosmochim. Acta 295, 155–177. https://doi.org/10.1016/j.gca.2020.12.006.
Stern, R.A., 2001. A New Isotopic and Trace-Element Standard for the Ion Microprobe: Preliminary Thermal Ionization Mass Spectrometry (TIMS) U-Pb and electron-Microprobe Data. Natural Resources Canada, Geological Survey of Canada Ottawa, ON, Canada.
Straub, S.M., Woodhead, J.D., Arculus, R.J., 2015. Temporal Evolution of the Mariana Arc: Mantle Wedge and Subducted Slab Controls Revealed with a Tephra Perspective. J. Petrol. 56, 409–439. https://doi.org/10.1093/petrology/egv005.
Styles, M., Ellison, R., Arkley, S., Crowley, Q.G., Farrant, A., Goodenough, K.M., McKervey, J., Pharaoh, T., Phillips, E., Schofield, D., 2006. The geology and geophysics of the United Arab Emirates. Volume 2. 351pp. British Geological Survey, Nottingham.
Tang, Y.-J., Zhang, H.-F., Ying, J.-F., 2007. Review of the Lithium Isotope System as a Geochemical Tracer. Int. Geol. Rev. 49, 374–388. https://doi.org/10.2747/0020-6814.49.4.374.
Teng, F.-Z., McDonough, W.F., Rudnick, R.L., Dalpé, C., Tomascak, P.B., Chappell, B.W., Gao, S., 2004. Lithium isotopic composition and concentration of the upper continental crust. Geochim. Cosmochim. Acta 68, 4167–4178. https://doi.org/10.1016/j.gca.2004.03.031.

Teng, F.-Z., McDonough, W.F., Rudnick, R.L., Walker, R.J., Sirbescu, M.-L.C., 2006. Lithium isotopic systematics of granites and pegmatites from the Black Hills, South Dakota. Am. Mineral. 91, 1488–1498. https://doi.org/10.2138/am.2006.2083.

Tilton, G.R., Hopson, C.A., Wright, J.E., 1981. Uranium-lead isotopic ages of the Samail Ophiolite, Oman, with applications to Tethyan Ocean ridge tectonics. J. Geophys. Res. Solid Earth 86, 2763–2775. https://doi.org/10.1029/JB086iB04p02763.

Tomascak, P.B., 2004. Developments in the Understanding and Application of Lithium Isotopes in the Earth and Planetary Sciences. Rev. Mineral. Geochem. 55, 153–195. https://doi.org/10.2138/gsrmg.55.1.153.

Tomascak, P.B., Tera, F., Helz, R.T., Walker, R.J., 1999. The absence of lithium isotope fractionation during basalt differentiation: new measurements by multicollector sector ICP-MS. Geochim. Cosmochim. Acta 63, 907–910. https://doi.org/10.1016/S0016-7037(98)00318-4.

Tsuchiya, N., Shibata, T., Yoshikawa, M., Adachi, Y., Miyashita, S., Adachi, T., Nakano, N., Osanai, Y., 2013. Petrology of Lasail plutonic complex, northern Oman ophiolite, Oman: an example of arc-like magmatism associated with ophiolite detachment. Lithos 156–159, 120–138. https://doi.org/10.1016/j.lithos.2012.10.013.

Valley, J.W., 2003. Oxygen isotopes in zircon. Rev. Mineral. Geochem. 53. https://doi.org/10.2113/0530343.

Valley, J.W., Lackey, J.S., Cavosie, A.J., Clechenko, C.C., Spicuzza, M.J., Basei, M.A.S., Bindeman, I.N., Ferreira, V.P., Sial, A.N., King, E.M., Peck, W.H., Sinha, A.K., Wei, C. S., 2005. 4.4 billion years of crustal maturation: Oxygen isotope ratios of magmatic zircon. Contrib. Mineral. Petrol. 150, 561–580. https://doi.org/10.1007/s00410-005-0025-8.

Vermeesch, P., 2018. IsoplotR: a free and open toolbox for geochronology. Geosci. Front. 9, 1479–1493.

Vervoort, J.D., Plank, T., Prytulak, J., 2011. The Hf–Nd isotopic composition of marine sediments. Geochim. Cosmochim. Acta 75, 5903–5926. https://doi.org/10.1016/j.gca.2011.07.046.

Warren, C.J., Parrish, R.R., Waters, D.J., Searle, M.P., 2005. Dating the geologic history of Oman's Semail ophiolite: Insights from U-Pb geochronology. Contrib. Mineral. Petrol. 150, 403–422.

White, W.M., 2015. Isotope Geochemistry. John Wiley & Sons, New York.

Whitehead, J., Dunning, G.R., Spray, J.G., 2000. U-Pb geochronology and origin of granitoid rocks in the Thetford Mines ophiolite, Canadian Appalachians. Geol. Soc. Am. Bull. 112, 915–928.

Wiedenbeck, M., Alle, P., Corfu, F.Y., Griffin, W.L., Meier, M., Oberli, F.V., Quadt, A., Roddick, J.C., Spiegel, W., 1995. Three natural zircon standards for U-Th-Pb, Lu-Hf, trace element and REE analyses. Geostand. Newslett. 19, 1–23.

Wiedenbeck, M., Hanchar, J.M., Peck, W.H., Sylvester, P., Valley, J., Whitehouse, M., Kronz, A., Morishita, Y., Nasdala, L., Fiebig, J., Franchi, I., Girard, J.-P., Greenwood, R.C., Hinton, R., Kita, N., Mason, P.R.D., Norman, M., Ogasawara, M., Piccoli, P.M., Rhede, D., Satoh, H., Schulz-Dobrick, B., Skår, O., Spicuzza, M.J., Terada, K., Tindle, A., Togashi, S., Vennemann, T., Xie, Q., Zheng, Y.-F., 2004. Further Characterisation of the 91500 Zircon Crystal. Geostand. Geoanal. Res. 28, 9–39. https://doi.org/10.1111/j.1751-908X.2004.tb01041.x.

Williams, K.L., 1987. An Introduction to X-Ray Spectrometry: X-Ray Fluorescence and electron Microprobe Analysis. Allen & Unwin Boston, Massachusetts.

Wilson, M., 1989. Igneous petrogenesis. Springer.

Woodhead, J.D., Hergt, J.M., Davidson, J.P., Eggins, S.M., 2001. Hafnium isotope evidence for 'conservative' element mobility during subduction zone processes. Earth Planet. Sci. Lett. 192, 331–346. https://doi.org/10.1016/S0012-821X(01)00453-8.

Xia, X.-P., Cui, Z.-X., Li, W., Zhang, W.-F., Yang, Q., Hui, H., Lai, C.-K., 2019. Zircon water content: reference material development and simultaneous measurement of oxygen isotopes by SIMS. J. Anal. At. Spectrom. 34, 1088–1097. https://doi.org/10.1039/C9JA00073A.

Yakymchuk, C., Kirkland, C.L., Clark, C., 2018. Th/U ratios in metamorphic zircon. J. Metamorph. Geol. 36, 715–737. https://doi.org/10.1111/jmg.12307.

You, C.-F., Chan, L.-H., 1996. Precise determination of lithium isotopic composition in low concentration natural samples. Geochim. Cosmochim. Acta 60, 909–915. https://doi.org/10.1016/0016-7037(96)00003-8.

Zack, T., Tomascak, P.B., Rudnick, R.L., Dalpé, C., McDonough, W.F., 2003. Extremely light Li in orogenic eclogites: the role of isotope fractionation during dehydration in subducted oceanic crust. Earth Planet. Sci. Lett. 208, 279–290. https://doi.org/10.1016/S0012-821X(03)00035-9.

Zhang, W., Hu, Z., 2020. Estimation of isotopic reference values for pure materials and geological reference materials. At. Spectrosc. 41, 93–102.

Zhang, G., Zhang, J., Wang, S., Zhao, J., 2020. Geochemical and chronological constraints on the mantle plume origin of the Caroline Plateau. Chem. Geol. 540, 119566. https://doi.org/10.1016/j.chemgeo.2020.119566.

Zhang, H., Tian, S., Wang, D., Li, X., Liu, T., Zhang, Y., Fu, X., Hao, X., Hou, K., Zhao, Y., Qin, Y., 2021. Lithium isotope behavior during magmatic differentiation and fluid exsolution in the Jiajika granite–pegmatite deposit, Sichuan, China. Ore Geol. Rev. 134, 104139. https://doi.org/10.1016/j.oregeorev.2021.104139.